ABSTRACT

Thermal / Structural Analysis of the HB 650 Thermal Shield

Gerald J. Smith, MS
Mechanical Engineering
Northern Illinois University, 2020
Iman Salehinia, Director

Fermilab's PIP-II project's superconducting linear accelerator will drive the next generation of particle accelerators through a revolution in beam intensity. Key to beam intensification are the high efficiencies of niobium-tin superconducting radiofrequency (SRF) cavities operating at cryogenic temperatures near 5 Kelvin. A multifaceted approach is employed to achieve and maintain the extreme temperature. Vacuum provides the first barrier to thermal convection. Physical thermal intercept zones further isolate the exterior shell vacuum vessel at 300 Kelvin from the supercooled beamline. The first thermal intercept lies just inside the exterior vacuum vessel forming the 40 Kelvin zone. This 40K thermal shield is the focus of this investigation.

In preparation for operation, the thermal shield is cooled from 300K to 40K in a slow process over 2-1/2 days. The factors limiting the cooling rate are a high thermal gradient which produces thermal strain and high mechanical stress. Decreasing the time required to reach operational temperatures is the desired research goal.

Physical testing data and finite element method (FEM) computer models from the Single Spoke Resonator – 1 (SSR1) and Linac Coherent Light Source (LCLS-II) cryomodules will be evaluated to determine needed design changes. The thermal shield design for the High Beta 650 MHz (HB650) will be modified and analyzed using FEM computer models to determine maximum cooling rate with a target of 50 thermal cycles of life. Maximum allowable stress will be determined through low cycle fatigue calculations.

NORTHERN ILLINOIS UNIVERSITY
DE KALB, ILLINOIS

DECEMBER 2020

THERMAL / STRUCTURAL ANALYSIS OF THE HB 650 THERMAL SHIELD

BY

GERALD J. SMITH

A THESIS SUBMITTED TO THE GRADUATE SCHOOL

IN PARTIAL FULFILLMENT OF THE REQUIREMENTS

FOR THE DEGREE

MASTER OF SCIENCE

DEPARTMENT OF MECHANICAL ENGINEERING

Thesis Director:
Iman Salehinia

Table of Contents

List of Tables

List of Figures

List of Equations

This document was prepared by Gerald J. Smith using the resources of the Fermi National Accelerator Laboratory (Fermilab), a U.S. Department of Energy, Office of Science, HEP User Facility. Fermilab is managed by Fermi Research Alliance, LLC (FRA), acting under Contract No. DE-AC02-07CH11359.

Chapter 1: Introduction

Fermilab's Proton Improvement Plan Part 2 (PIP-II) project's superconducting linear accelerator (LINAC) will drive the next generation of particle accelerators through a revolution in beam intensity. Construction of the new LINAC tunnel and above-ground laboratory began in March 2019. Groundbreaking for the new cryoplant building that will house the equipment producing cryogenically cooled gases and supercooled liquified helium occurred in July 2020. The first section of the accelerator chain operates at room temperature and will allow scientists to perform multiple experiments operating simultaneously. The first stage of construction will open for physics research by the end of 2020. Figure 1 shows current and proposed Fermilab beamlines. [1]

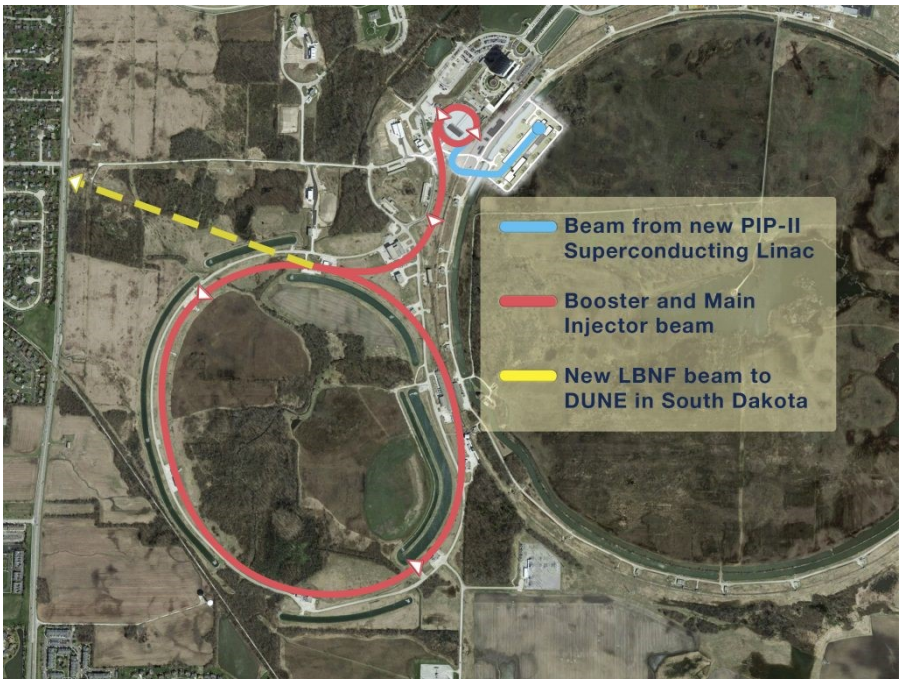

Figure 1 - Aerial photo of Fermilab grounds with an overlay of the proposed beamlines. [1]

One of the many experiments fed by the beam from the new PIP-II LINAC will be the deep underground neutrino experiment (DUNE). Neutrinos rarely interact with matter, so producing a beam with large, concentrated particle bunch or high luminosity increases the number of events observed. One neutrino detector will be stationed at Fermilab and the other 550 miles away, in the Sanford Underground Research Facility in South Dakota, to measure changes in the particles as they travel. The beam of protons passes through a graphite rod called the target. The protons traveling near the speed of light crash into the graphite atoms and the explosion produces neutrons and pi mesons, also known as pions. Positively charged pions continue while all other subatomic particles are stripped from the beam. After 26 nanoseconds on average, charged pions decay into muons and neutrinos. The beam passes through a concrete barrier where the muons are absorbed, and the neutrinos pass through without interacting. [2]

Each new discovery allows scientists an opportunity to refine their theories and open new avenues for research. Researchers at the Super-Kamioka Neutrino Detection Experiment studying neutrino emissions from the sun were able to determine that neutrinos do have mass contrary to previous understanding of the standard model. [3] There is certainly more to be discovered about these ghost-like particles. The primary goals of the DUNE experiment are to refine the standard model and search for the unification of forces. Neutrinos could explain why the universe is made of matter. [2]

PIP-II will be designed and built in collaboration with domestic and international partner institutions in Great Britain, France, Italy, India, Poland, and the United States. Each partner provides specific technological expertise and in-kind contributions of hardware and technology to support design and construction. Once completed, the LINAC will be able to generate a proton beam greater than 1 megawatt traveling at a velocity up to 92% of the speed of light. Combined with future upgrades, this will triple Fermilab's current beam power. [1]

The LINAC will be 700 feet long consisting of several cryomodules. Figure 2 shows the quantity, type, and order of arrangement during operation. The beam originates from one of the ion sources shown on the right of the image. The accelerator will operate in either pulsed or continuous beam modes. In pulsed beam mode, particles are bunched, chopped, and focused into beam pulses before entering the first cryomodule, or cryogenically cooled vessel, the Half Wave Resonator (HWR). The HWR was produced by Argonne National Laboratory and delivered to FNAL in 2019. [1] A prototype of the Single Spoke Resonator – 1 (SSR1) cryomodule has completed construction and is currently being tested. The next prototype under development is the High Beta 650 (HB650), the primary subject of this thesis.

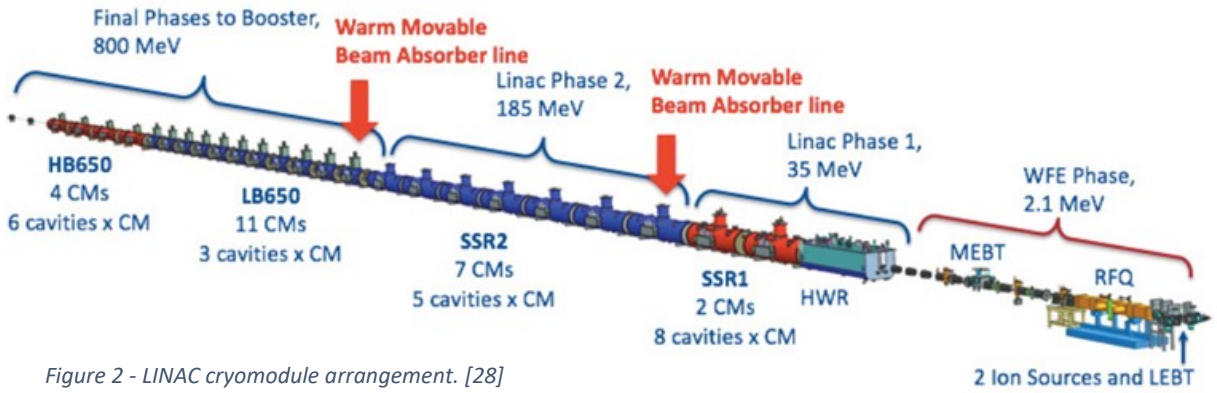

Figure 2 - LINAC cryomodule arrangement. [28]

Cryomodules that follow HWR have a similar exterior form and in fact have many common design elements. The biggest difference between these modules is the shape of the cavity. As the beam accelerates, new cavity geometry is required to optimize the electro-magnetic field for higher velocities and acceleration. The similarity between cryomodules extends beyond PIP-II. The LINAC Coherent Light Source (LCLS-II) being built for Stanford Linear Accelerator Center (SLAC) uses free electrons as the ion source and is used to produce intense x-ray beams, but the design of cryomodules is very similar. This similarity extends to a wide variety of cryogenically cooled particle accelerators across the globe.

Figure 3 is a photograph of the nearly complete SSR1 prototype cryomodule. The most notable feature is the red vacuum vessel. This exterior shell remains at room temperature but provides the first obstacle to heat transfer to the supercooled beamline. Vacuum precludes transmission of heat energy between the exterior shell and air molecules to interior components. Several bolted and sealed flange ports through the vacuum vessel wall provide access. There are eight RF power couplers, one for each cavity inside the vessel, although only two power couplers are fully assembled as shown in the image. The eight instrument connection ports have multiple bulkhead wire connectors for control and monitoring devices such as transducers for temperature, pressure, and helium liquid level, as well as tuner motor power and control. [1]

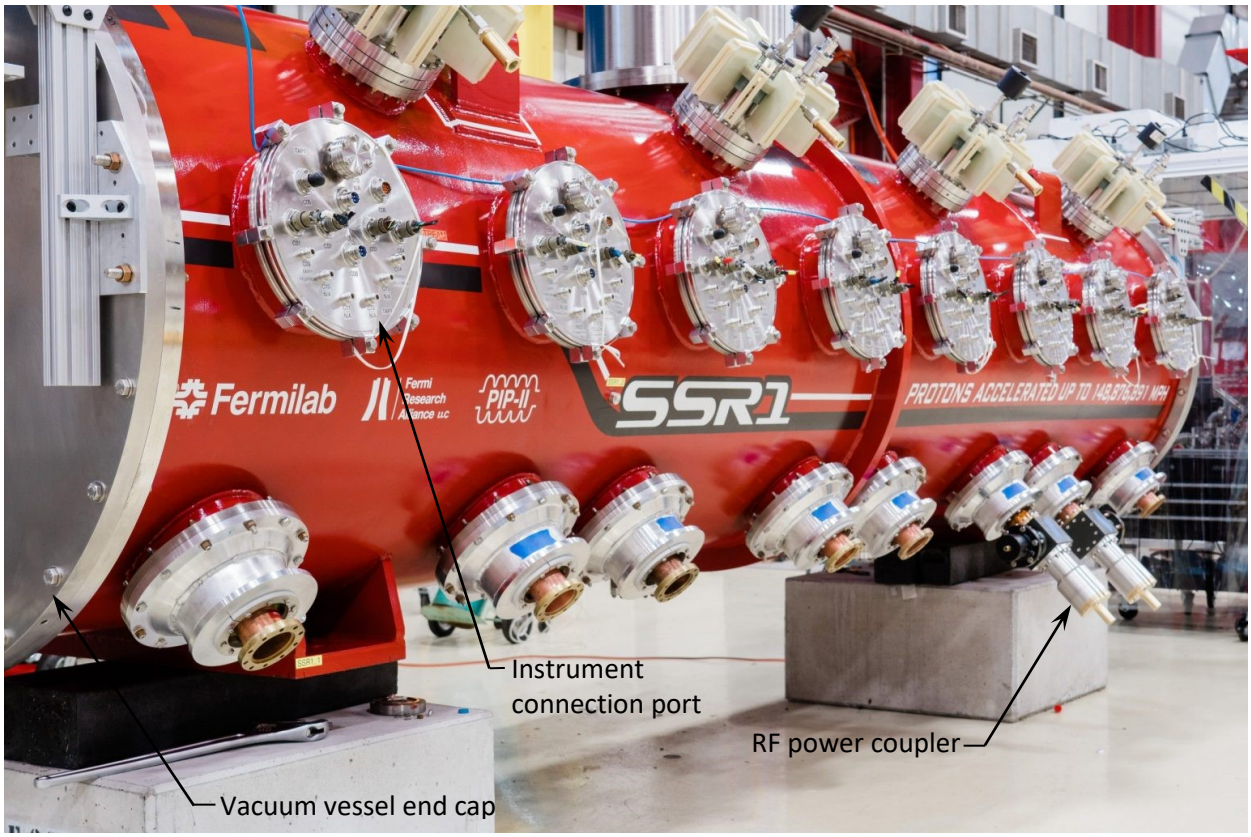

Figure 3 - SSR1 prototype cryomodule exterior [27]

A computer model rendering with a cut-away window illustrates the internal components of the SSR1 prototype in Figure 4. Each SRF cavity has a tuner and an interstitial chamber for liquid helium. Niobium becomes a superconductor at temperatures below 9.2 Kelvin, which increases the quality of the EM field produced. Liquid helium provides the extremely low temperatures required and the liquid helium chamber will be completely filled during operation to cool every surface of the niobium SRF cavity. The tuner applies force to change the physical shape of the cavity to focus the electro-magnetic field that accelerates the proton beam. [1]

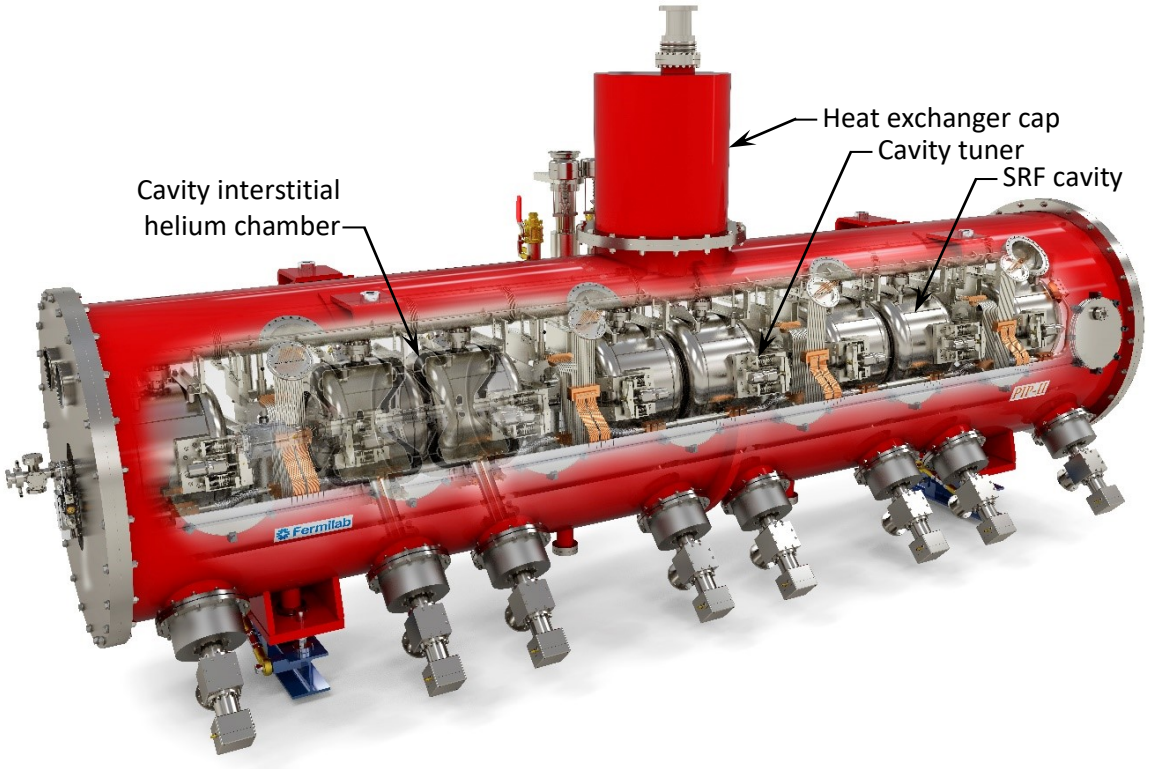

Figure 4 - SSR1 Prototype cryomodule with cut-away view. [25]

Helium at atmospheric temperatures evaporates from liquid to gas at 3.7 Kelvin. If held under vacuum, the boiling point can be reduced as low as .3 Kelvin. There are two thermal zones closest to the

beamline, 5 Kelvin and 2 Kelvin. The 5 Kelvin intercept is cooled by helium through a phase change from liquid to gas. At pressures below 5 kPa near the saturation line between liquid and gas phases, liquid helium takes on new characteristics. Cryonicists refer to these two liquid phases as He-I and He-II. He-I is the warmer and behaves like normal fluids. He-II is called a superfluid due to some unusual physical properties. He-II seems to have no viscosity or enthalpy and all heat energies are the normal component. If pressure is higher than 5 kPa and heat is added, He-II transforms to He-I. If pressure is below 5 kPa, He-II changes to vapor with the addition of heat. The phase diagram of helium is provided in Figure 5. [4]

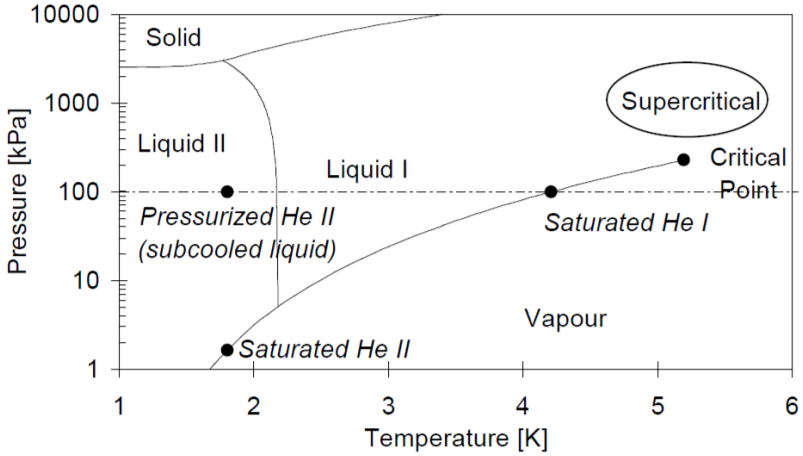

Figure 5 - Phase diagram of helium [4]

The cost in terms of electricity, hardware, and systems increases as the temperature of helium decreases. With the vacuum vessel at room temperature, around 296 Kelvin, and the cavities supercooled to 2 Kelvin, radiant and conductive heat transfer would be very large. To mitigate radiation and conduction heat transfer to the cavities, two physical intercept zones are established. The inner 5K zone absorbs conducted heat energy and the 35-50K thermal shield absorbs conducted and radiant heat from the vacuum vessel. Additional radiation mitigation is achieved by wrapping the beamline

components with multiple layers of insulation (MLI) as a break between 35-50K and 2K. MLI is also wrapped outside the thermal shield panels as a break between 296K and 35-50K. The secondary goal, after 2K beamline temperature, is to economize power and conserve resources by maximizing heat removal at 35-50K and again at 5K to minimize the thermal load at 2K.

Figure 6 is a detailed view of the Fermilab HB650 NX CAD model showing how the thermal intercept zones isolate the first cavity. Note the MLI is not shown. Each intercept is connected to the heat exchanger with a copper, braided-wire thermal strap with nuts, bolts, and Belville washers.

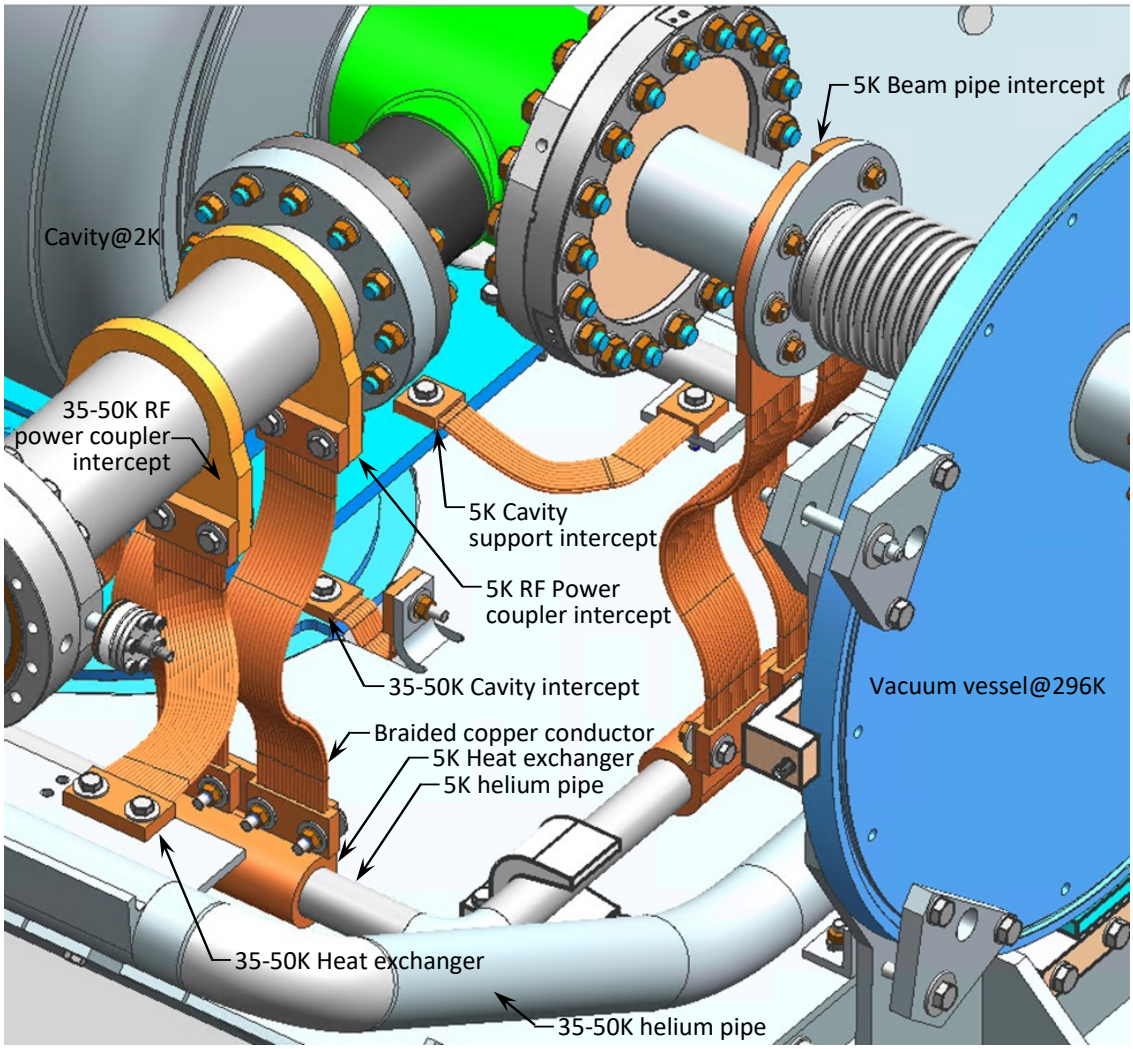

Figure 6 - Thermal intercept zones for HB650. (Image acquired from Fermilab HB650 NX CAD model)

A photograph of SSR1 during construction is shown in Figure 7. Silver MLI can be seen wrapping around two cavities and the 5K helium pipe. Instrumentation wiring with special white insulation due to the extreme cold, vacuum, and radioactive environment connect several devices in the image. Wires labeled “Sensor wire” disappear through MLI to be connected to devices monitoring cavity conditions. Cryogenic cooling and thermal intercept strategy and design for SSR1 and HB650 are very similar.

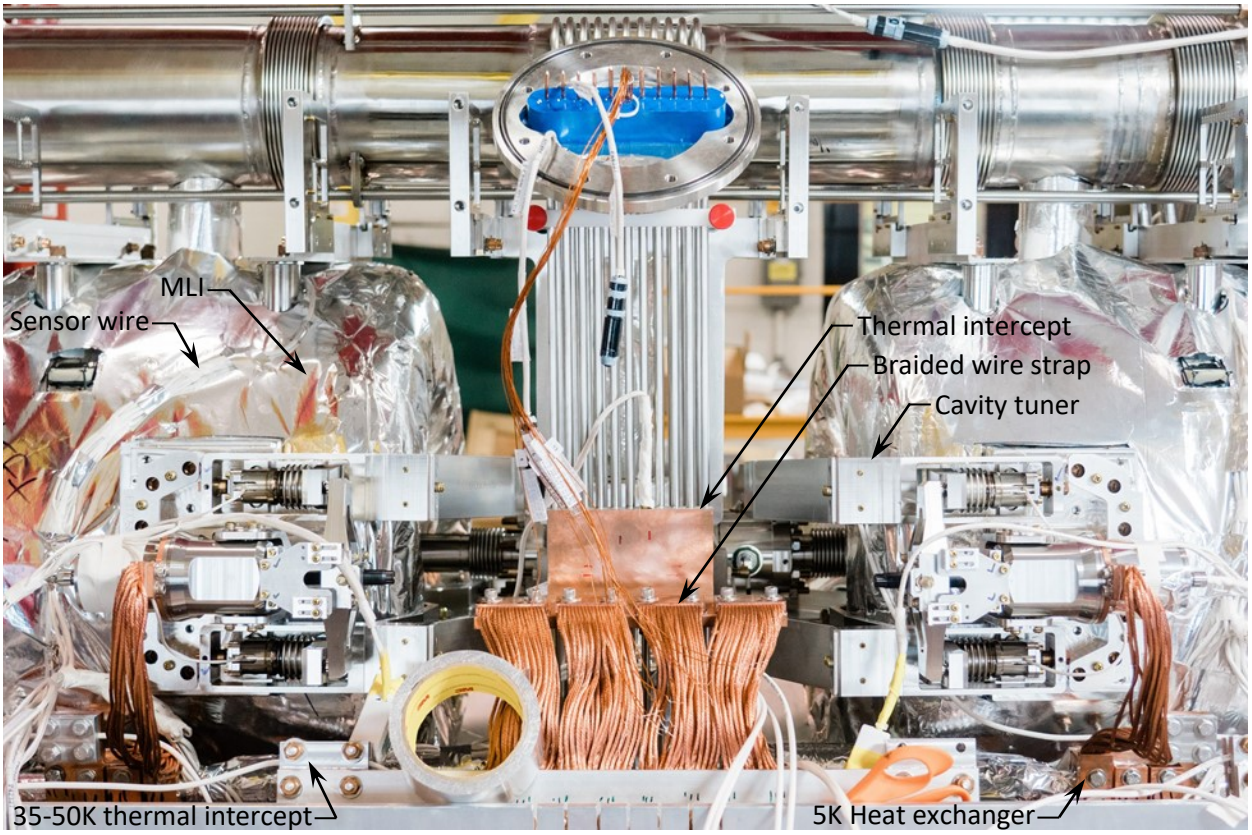

Figure 7 - SSR1 cold mass and thermal intercept details. [26]

Radiant heat intercept panels on the 35-50K thermal shield are welded to flanges on the heat exchange pipe. SSR1 and LCLS-II shield panels and heat exchange pipe flanges have slits between and perpendicular to 25mm long weld beads. The resulting geometry has been given the name “fingers” or “finger welds” due to the likeness. An engineer at Fermilab stated these finger welds have been in use

on cryomodule thermal shields for 30 years or more. [5] Figure 8 shows the thermal shield for SSR1 [6] and a detail view of finger weld geometry and a photograph of welds are shown in Figure 9.

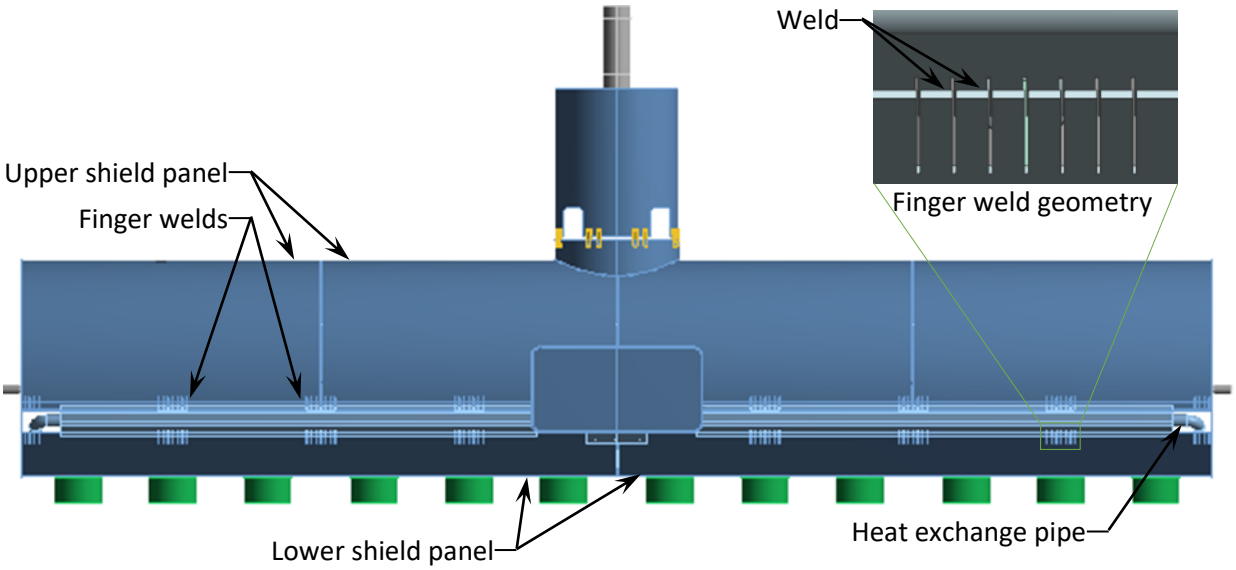

Figure 8 - SSR1 thermal shield [6]

Figure 9 - Finger welds

Significant amounts of design, analysis and testing data for the current models are available. This thermal shield design strategy is currently being used on LCLS-II and the prototype SSR1 cryomodules in production today. The maximum allowable cooling rate for LCLS-II has been established to be 10 Kelvin

per hour and SSR1 to be 5 Kelvin per hour. Approaching the prototype High Beta 650 MHz (HB 650), one of the international partners, the Indian national laboratory, Raja Ramanna Centre for Advanced Technology (RRCAT), was asked to evaluate and modify the design to achieve a cooling rate of 20 Kelvin per hour or greater. The RRCAT design proposal employed a strategy similar to current models with an allowable cooling rate of 7.67 Kelvin per hour. [7]

Following RRCAT's proposal, a request was made to review the current design strategy, and additional proposals were sought for an updated design. Cryomodule prototype design had commenced and was mature, so modifications were to be limited in scope due to the impact on other cryomodule components. The specifications for design included preliminary physical dimensions for the device, a requirement for a minimum of 50 thermal cycles, and helium gas refrigerant. A cooling cycle was defined as starting at room temperature, cooling to operating temperatures, and then warming to room temperature again. Additionally, a cooling rate, defined as a change in temperature of the supplied helium gas refrigerant from 296K to 40K, was to be 20 Kelvin per hour or greater.

Previous work has been reviewed and additional analysis performed. Due to the similarities between cryomodules, only one received additional in-depth study. Newly performed analysis of SSR1 became the basis for the redesigned system that has been employed on HB650. That original work will be reviewed as we develop the problem statement and discuss the updated design strategy. Detailed analysis of the new HB650 thermal shield will then be presented.

Chapter 2: Problem Statement

Generally, matter expands when heated and contracts when cooled. There are a few exceptions to this rule of thumb though. Some polymers and ceramics shrink when heated due to a change in their molecular structure. Similarly, an increase in the temperature of water that results in a change in state from solid to liquid results in a decrease in volume. This change in dimension is defined as thermal strain. Engineers often must design to mitigate the effects of thermal strain or use thermal strain to accomplish a desired effect. Without thermal strain we would not have modern devices like hot air balloons, thermometers, steam turbines, internal combustion engines, rockets, and many more!

If an object undergoing a change in temperature is free to grow and temperature within the object remains uniform, then little, or no mechanical stress will be developed. Sudden or uneven changes in temperature can cause mechanical stress to rise. If you pour a warm liquid over a large ice cube, the cube might pop and crack. The core of the cube remains cold, but the surface temperature rises quickly. When the difference in thermal stress and strain within the cube rises beyond its strength, it will fracture. Slow changes in temperature can also cause failure if growth is constrained. Diurnal and seasonal changes in temperature cause roads, buildings, and other structures to change size. Typically, these structures are built with expansion joints to prevent failure. Occasionally, on days of extreme heat, roadways still rupture.

The HB650 thermal shield is cooled by helium gas refrigerant flowing through a heat exchange pipe. The pipe is cooled by convection, and diffusion draws heat by conduction into the pipe. As the thermal shield cools, heat is drawn in from the environment by radiation and conduction. As the cooling rate increases, the thermal gradient increases. Higher thermal gradient increases the temperature

differences between structural members, which means different thermal displacement that drives mechanical strain and stress. Mechanical stress and strain are the limiting factors and when exceeded, failure will occur.

Cavity support posts are mounted to a structure called “strongback”, a mechanical beam that is intended to hold the cavities and beamline in a fixed position. Cavity support posts also support the thermal shield. The strongback remains outside the cold zones inside the vacuum vessel. Cavity support posts are made from fiber-reinforced epoxy with high thermal insulation value. Some heat conduction does occur, but the temperature change in the strongback has been calculated to be less than 4 Kelvin by another Fermilab engineer. During cryomodule cooldown, the aluminum thermal shield shrinks. The connection between the thermal shield and a central cavity support post are made with nuts, bolts, and Belleville washers to provide one fixed reference point. The seven remaining cavity support posts have shoulder bolts with slots to accommodate the differences in temperature as shown in Figure 10.

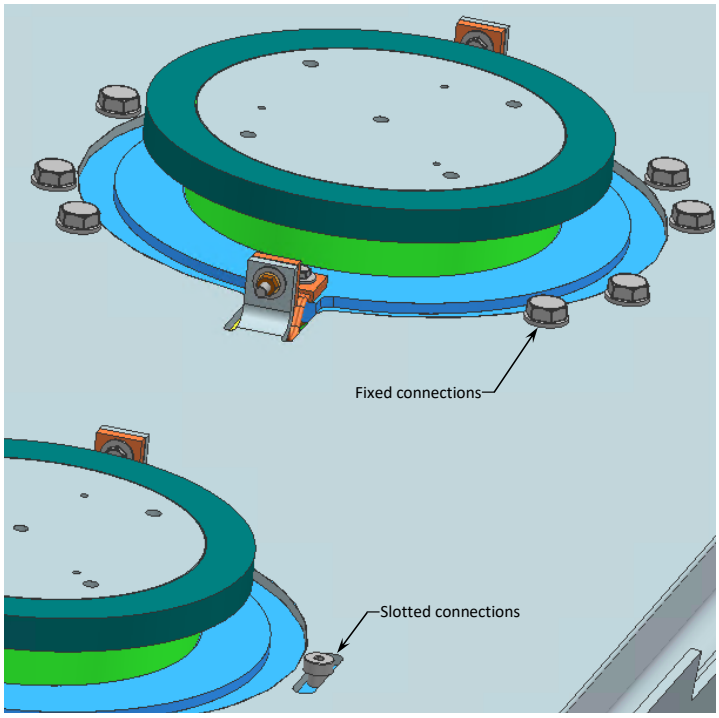

Figure 10 - Thermal shield mounting scheme (Image acquired from Fermilab NX CAD model.)

The thermal shield is free to contract without outside restrictions. Examination of temperature differences between structural members of the shield provides a clear visual of the problem. Figure 11 is a snapshot in time of the transient cooldown process from an Ansys simulation of SSR1. The selected time of this image corresponds to the moment when stress and strain peak. The heat exchange pipe is the coldest member, and the temperature of the panels is higher. The difference in temperature equates to a difference in thermal contraction, otherwise known as displacement. Displacement drives mechanical strain which drives stress. I will use FEA simulation to obtain the temperature map, displacement field, mechanical strain field, and mechanical stress field. The new design will be discussed, and the same analysis will be performed. This will be compared to the strength of materials and fatigue-life calculated.

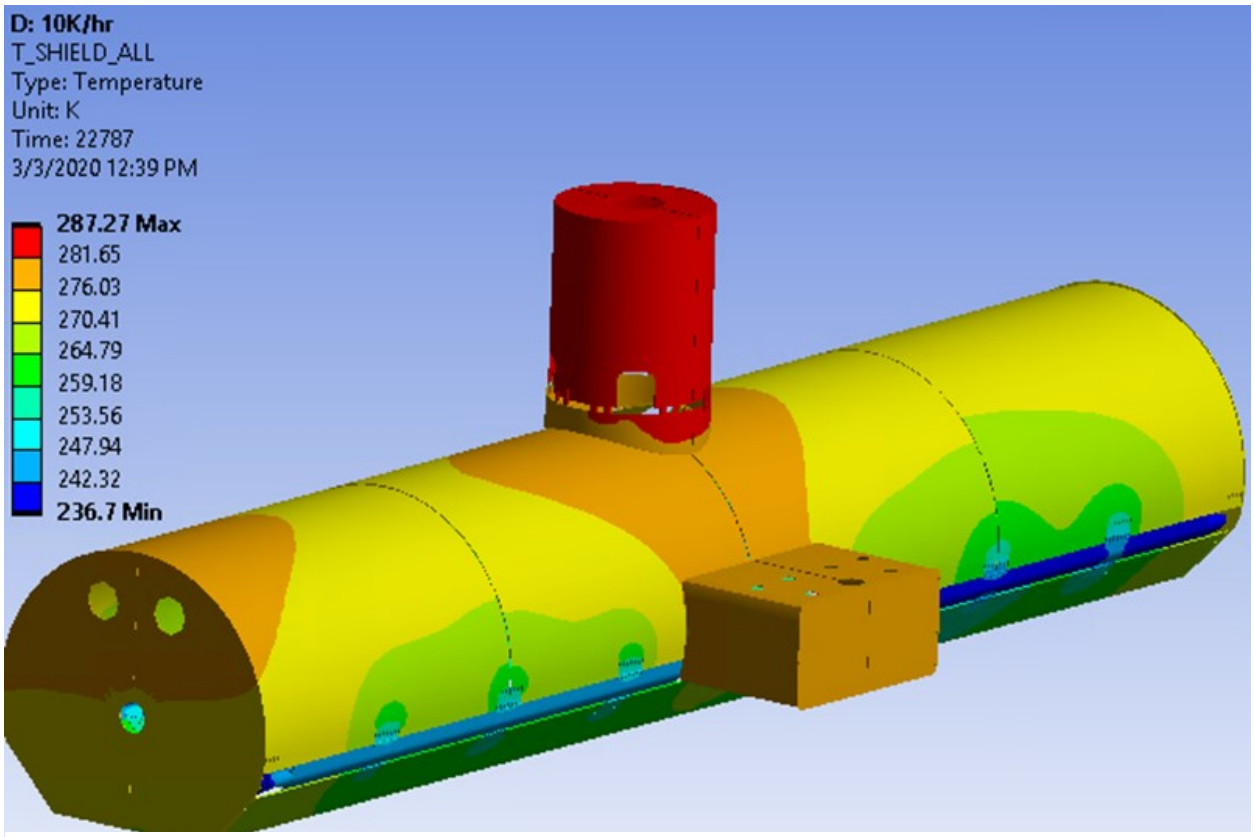

Figure 11 - Temperature distribution map of SSR1 at the moment of greatest stress (5K/hr) (Image acquired from Ansys.)

Chapter 3: Methods

3.1 Methods Introduction

In this chapter we will discuss the specific techniques used for analysis. The material of each component of the structure will be discussed in detail as well as the effect of welding on those materials. The materials discussion will lead into the discussion of mechanical-structural stress-strain assumptions and computation. This will lead to a discussion of strain energy density and equivalent strain energy density methods with application to finite element analysis. With the discussion of mechanical methods complete, we will move into the discussion of thermophysical properties of the solids in the structure as well as the helium gas refrigerant. Thermophysical properties will transition to mathematical concepts for heat transfer and application in the FEA model.

These analysis methods will then be applied to the SSR1 thermal shield and new results shown. New results from SSR1 have guided the design of the thermal shield system for HB650. Three similar designs for HB650 will be proposed and discussed. Proposed geometry, created using Siemens NX CAD software, has been imported into Ansys, simplified, and discretized. Boundary conditions, convection features for the helium refrigerant, and radiation features for thermal analysis will be described. The process of passing transient thermal temperature maps to static structural simulations and structural boundary conditions will also be presented.

3.2 Materials of Construction

The thermal shield system can be subdivided into three broad subsystems. The helium heat exchange pipe is composed of pipe sections and fittings butt welded together to form one continuous duct. The pipe includes three sections of custom-extruded profile with three integral flanges for attachments. The upper and lower shield panels will be welded to two of these flanges. Thermal intercept blocks will be attached to the third flange using nuts and bolts. Prior to welding, these three sections of custom extrusion are CNC machined to add the mounting holes and clearance features required in the finished weldment. Once welded, the completed pipe is pressure tested for leaks.

The helium heat exchange pipe and fitting components are made from 6061-T6 aluminum. Butt welds are produced using gas tungsten arc welding (GTAW), also known as tungsten inert gas (TIG) welding, which is an arc welding process that uses a non-consumable tungsten electrode to produce the weld. A consumable rod of 4043 is used in the welding process to add filler material to the joint and improve strength.

The second and third subsystems are then added to the finished helium heat exchange pipe. Sheet metal panels are formed and pre-machined. The purpose of these panels is to block outside thermal radiation from reaching the supercooled beamline. One set of panels will remain permanently attached, while the other can be removed for access to internal components if required. For LCLS-II, the upper shield sections are permanently attached, and for SSR1 and HB-650, the lower shield sections are permanent. The permanent shield sections are lap welded in place while the removable sections are dry fit for quality check only. The helium heat exchange pipe and permanent shield weldment will be assembled to the beamline. The beamline will be completely assembled and insulated before the removable sections of thermal shield are welded to the helium heat exchange pipe.

All sheet metal panels, whether removable or permanently fixed, are made from 1100-H14 aluminum, selected for its high thermal conductivity. Shield panels are attached by weld to the flanges of the helium heat exchange pipe using the GTAW process with 4043 filler rod. Multiple fillet welds connect shield panel edges to the attachment flange face. If a panel must be removed, the fillet welds are cut and ground smooth. Reattaching the panel is accomplished by repeating the same GTAW process over the same edges and surfaces.

1100 aluminum is commonly referred to as commercially pure aluminum. The chemical composition specification requires a minimum of 99.00% aluminum and the remainder considered impurities. The chemical makeup does not provide a means for hardening by thermal heat treatment. The mechanical properties can however be modified through work hardening, also known as strain hardening. The temper number following the 1100 grade indicates the amount of cold work and strain hardening that has been done to the raw material. In the annealed state, the temper number is denoted as 'O' (1100-O). The 'Hxx' designation refers to strain-hardened material. The two numerals indicate the type and amount of work done. The first numeral shows the type of work done and can be either '1' for strain hardened only or '2' for strain-hardened and partially annealed product. The second numeral shows the relative amount of work done on a scale from 1 through 8, with 8 being the highest temper normally produced. [8] Often these temper numbers are referred to as 2-quarter hard, 4-half hard, and 8-full hard. Note, the 1100-H14 sheet aluminum has been further cold worked to form the shield panels.

4043 is an alloy commonly used as filler material during welding. The high silicon content reduces the melting point, ensuring the filler material will liquify completely before the base materials. This low melting point makes 4043 ideal for welding processes. 4043 does not have alloying elements in significant quantities to allow for heat treatment. The mechanical properties can be modified through strain hardening and the temper designations of 'O' and 'Hxx' can be applied. [8] During welding, the

filler metal is completely liquified, so the temper before processing is irrelevant. Welding liquifies a portion of the base material, which mixes with the filler material. The resulting alloy within the weld nugget may be hardened through thermal heat treatment depending upon the chemistry of the alloy mixture. For our application, the thermal shield will not be heat treated after welding.

6061 aluminum alloy is heat treatable through precipitation hardening. The primary alloying elements that allow hardening are magnesium and silicon, which forms magnesium silicate. The temper designation following the 6061 grade can be either 'O' for annealed or 'Txxx' denoting the thermal heat treatment process or temper state. [8] 6061 extruded aluminum is quickly cooled or quenched after exiting the extrusion die to achieve a T4 temper. Further thermal heat treatment increases the hardness to a maximum temper of T6. Additional tempers can be achieved using a variety of processes beyond the scope of this project. The annealed 'O' temper and hardened 'T6' temper will be evaluated during this investigation. Chemical composition specifications for each of the three grades of aluminum are shown in Table 1. [9]

Table 1 - Chemical Composition of Aluminum Alloy [9]

	1100		**4043**		**6061**	
	min %	max %	min %	max %	min %	max %
Aluminum (Al)	99	100	92.3	95.5	95.8	98.6
Beryllium (Be)	0	0.0008	0	0.0008	--	--
Chromium (Cr)	--	--	--	--	0.04	0.35
Copper (Cu)	0.05	0.2	0	0.3	0.15	0.4
Iron (Fe)	0	0.95[1]	0	0.8	0	0.7
Magnesium (Mg)	--	--	0	0.05	0.8	1.2
Manganese (Mn)	0	0.05	0	0.05	0	0.15
Silicon (Si)	0	0.95[1]	4.5	6	0.4	0.8
Titanium (Ti)	--	--	0	0.2	0	0.15
Zinc (Zn)	0	0.1	0	0.1	0	0.25
Other, each	0	0.05	0	0.05	0	0.05
Other, total	0	0.15	0	0.15	0	0.15

[1] Specifications for combined silicon and iron content in 1100 aluminum to be less than .95% total

Alloying elements and temper affect the yield and ultimate strength of aluminum. A compilation of engineering stresses, annealing temperature, and melting points are shown in Table 2. It is important to note the differences between engineering stress and true stress to avoid an apple/orange comparison. Engineering stress and strain are computed as applied force divided over the initial cross-sectional area. True stress accounts for the reduction in cross-sectional area due to strain and necking effects. Transforming engineering stress and strain to true stress and strain can be accomplished using the formulas:

$$\sigma_{true} = \sigma_{\text{engineering}} \left(1 + \varepsilon_{\text{engineering}}\right)$$

Equation 1 – Engineering stress – true stress relationship

$$\varepsilon_{true} = \ln\left(1 + \varepsilon_{\text{engineering}}\right)$$

Equation 2 – Engineering strain - true strain relationship

Table 2 - Aluminum Strength by Grade and Temper [9]

	Modulus of Elasticity	Yield Strength	Ultimate Tensile Strength	Annealing Temperature	Melting Point
	GPa	MPa	MPa	ºC	ºC
1100-O	68.9	34.5	105	343	643
1100-H12	68.9	103	130	343	643
1100-H14	68.9	117	145	343	643
1100-H16	68.9	138	145	343	643
1100-H18	68.9	152	165	343	643
4043-O	N/A	70	145	349	573
6060-O	68.9	48.3	117	415	582
6061-T6	68.9	276	310	415	582

Welding liquifies the filler rod and some of the base metal. Effects from this high-temperature process affect the temper and strength of the surrounding unmelted base metals as well. This zone of reduced strength is known as the heat affected zone (HAZ). The Aluminum Design Manual states, “The as-welded strength of aluminum filler alloys without post-weld heat treatment depends only on their

chemical composition since the heat of welding erases cold-work. The chemical composition in the as-welded condition depends not only on the chemical composition of the filler but also on the base metal, since there is some mixing of the base and filler metals in the weld." [8]

A study by R.R. Ambriz and D. Jaramillo examined the effect of welding and high heat on 6061-T6 and 7075-T651 Aluminum. Each sample was created with the same alloy base metal on both sides of the weld with 4043 filler rod for 6061 and 5356 filler rod for 7075. Local yield strength correlates with microhardness values obtained by instrumented indentation testing. A plot of measured hardness values and distance from the weld centerline is shown in Figure 12. Notice the weld metal is harder due to the silicon content of 4043 aluminum and the softest material is in the HAZ. This soft zone did not experience melting but was heated sufficiently for partial annealing to occur. Hardness measured across the face shown in Figure 13 indicates some variability in the change in hardness and the amount of local annealing that has occurred. This local variation could be anticipated as a result of the manual nature of the welding and distribution of heat during the process. [10]

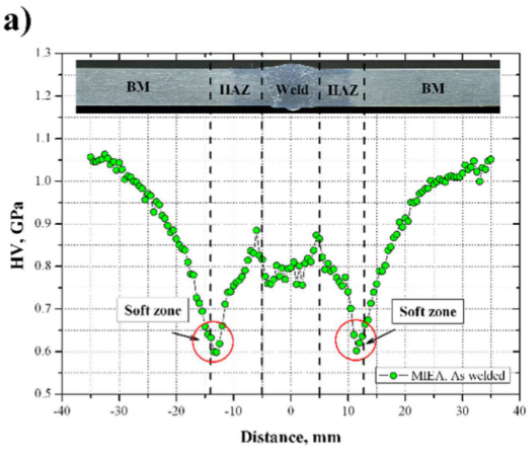

Figure 12 - Vickers hardness profile determined with 1 N of applied load throughout the welded joint [10]

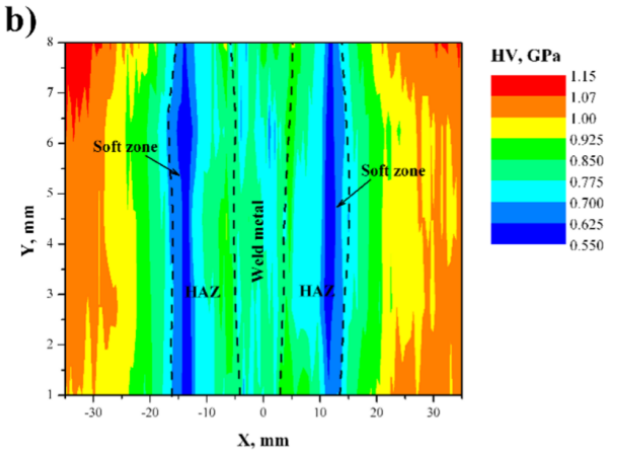

Figure 13 - Vickers Hardness map over the welded joint [23]

Vlademar Malin conducted a similar study of 6061-T6 weld joints and the metallurgical effects in the HAZ. Malin found a direct correlation between the area of minimum hardness in the HAZ and the location of tensile test failure regardless of welding variables. The hardness versus distance from the fusion line is overlaid with the location of failure during a tensile test is shown in Figure 15. A photo of the test specimen is shown in Figure 14. Notice the region of decreased hardness at the fusion line in Figure 15. The hardness at the fusion line in this sample was roughly 5% higher than the point of failure. Some specimens in Malin's study did have the lowest hardness at the fusion line or in the weld metal. In all cases, the location of failure during tensile testing corresponded with the minimum microhardness measured. [11]

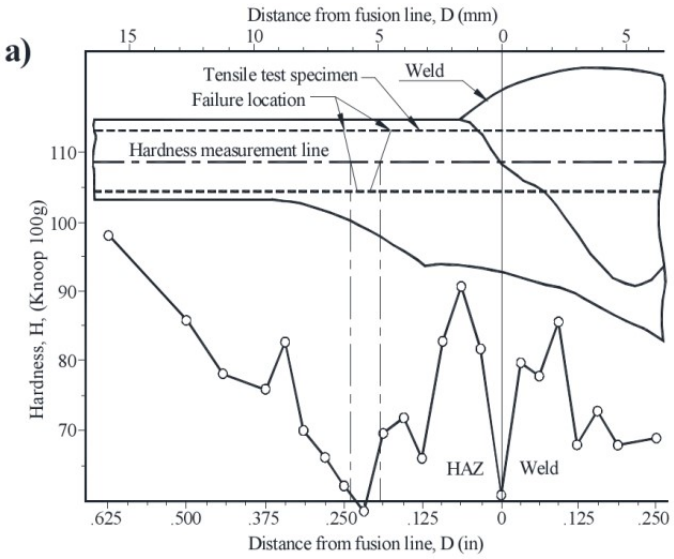

Figure 15 - Knoop hardness profile throughout the welded joint [11]

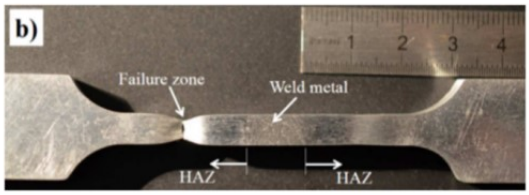

Figure 14 - Tensile test to failure specimen [11]

3.3 Mechanical Stress and Strain Computation

Let us begin with a brief discussion of how this type of problem would be solved using analytical methods and gather some important details about the FEA mathematical model. Forces can be thought of within two broad categories, body forces and surface forces. Body forces act upon mass or volume from a distance, as in gravity, magnetic, and electrical forces. Surface forces come from direct interaction between physical objects such as friction, tension, compression, torsion, hydrostatic pressure, air resistance, and the like. When a solid body or structure is subjected to any combination of body and surface forces, internal forces are developed and form a continuous function mathematically. Hooke's law governs the elastic region where a body returns its original shape when external forces are removed. The relationships between displacement, strain, and stress are linear in this region. The basic equations are Equation 3 relating stress and strain and Equation 4 relating strain and displacement.

$$\sigma_{ij} = C_{ijkl}\varepsilon_{ij}$$ *Equation 3 - Stress-strain*

$$\varepsilon_{ij} = \frac{1}{2}(u_{i,j} + u_{j,i})$$ *Equation 4 - Strain-displacement*

Which type of force does thermal strain fall into? A change in temperature results in a change in dimension of the material. Is the material isotropic or anisotropic? In other words, do the material properties change depending on direction? Wood, composites, fibers, and crystals tend to be anisotropic while metal and glass tend to be isotropic. Is the material homogeneous, having the same properties everywhere? Anisotropic and non-homogeneous materials might develop stress due to change in temperature and require analysis of the specific composition of the structure. Hooke's law with this type of thermal strain most likely does not apply. Thermal expansion for isotropic, homogeneous material with a volumetric, uniform change in temperature that can expand or contract unimpeded by surrounding objects develops little or no stress. When an obstacle is present, thermal

strain causes direct interactions between solid bodies. The forces generated through these physical interactions behave as surface forces. The thermal strain tensor can simply be added to the mechanical strain tensor as shown in Equation 5. [12]

$$\varepsilon_{ij}^{thermal} = \varphi_{ij}(T - T_0) \;\rightarrow\; \varepsilon_{ij}^{total} = \varepsilon_{ij}^{mechanical} + \varepsilon_{ij}^{thermal}$$ *Equation 5 - Thermal strain*

Above yield strength a new mathematical model is needed to express the association between stress and strain. Plastic deformation occurs, and the body undergoes permanent deformation. The relationships between displacement, strain, and stress are no longer linear. Currently the most common mathematical representation of the relationships between stress and strain is the Ramberg-Osgood method shown in Equation 6. [13]

$$\varepsilon^{total} = \varepsilon^{elastic} + \varepsilon^{plastic} = \frac{\sigma}{E} + \left(\frac{\sigma}{K'}\right)^{\frac{1}{n'}}$$ *Equation 6 - Ramberg-Osgood*

For the thermal shield application, the specifications require 50 cycles, which falls into a low cycle fatigue regime and plastic deformation will be assumed. FEA simulations often assume small deformation theory applied to material models in the linear-elastic region defined by Hooke's law. Non-linear material analysis for plastic deformation with large deformation theory could be employed. Aluminum is a homogeneous and isotropic material, but we have shown that it does not remain so when subjected to the high temperatures of welding. Localized softening reduces hardness, yield strength, and ultimate strength. This type of material non-linearity cannot be precisely simulated using commercially available FEA software.

Strain energy methods offer tools that can be used to solve stress-strain problems. As an introduction, consider the simple uniaxial loading condition within the linear-elastic region. Physical science defines work as force times distance or $W = \int F dx$. The energy (U) of work (W) will be stored

within the solid and will be completely recoverable when the force is released. A single stress element is shown in Figure 16. Stress (σ) acts upon the entire object, causing displacement (u) throughout its length and an infinitesimal change in the infinitesimal length of the element ($\frac{\partial u}{\partial x}dx$). Stress (σ) multiplied by the area of the face (dydz) is the force applied to the element shown in both the positive and negative directions along the x-axis. Equation 7 shows the relationship between work and strain energy through a balance of forces. Expanding terms and a little cleaning up on the right-hand side of the equation gives Equation 8. The definition of strain (ε_x) is the partial derivative of displacement $\left(\frac{\partial u}{\partial x}\right)$, and we can substitute the Hooke's law relationship between stress and strain ($\varepsilon_x = \frac{\sigma_x}{E}$) for this term as shown in Equation 9. Total strain energy (dU) for the stress element divided by the volume of the element (dxdydz) gives strain energy density. Hooke's law substitutions provide several useful relationships shown in Equation 10. Also notice that $\frac{\sigma_x \varepsilon_x}{2}$ is the area under the curve on a stress-strain plot as shown in Figure 17. [12]

$$\int F dx = dU = \int_0^{\sigma_x} \sigma dy dz \;\; d\left(u + \frac{\partial u}{\partial x}dx\right) - \sigma dx dy du$$

Equation 7 - Strain energy force balance

$$dU = \int_0^{\sigma_x} \sigma \;\; d\left(\frac{\partial u}{\partial x}\right) dx dy dz + \cancel{\sigma dy dz du} - \cancel{\sigma dx dy du}$$

Equation 8 - Strain energy simplification

$$dU = \int_0^{\sigma_x} \sigma \left(\frac{d\sigma}{E}\right) dx dy dz = \frac{\sigma_x^2}{2E} \; dx dy dz$$

Equation 9 - Strain energy solution

$$U = \frac{\sigma_x^2}{2E} = \frac{E\varepsilon_x^2}{2} = \frac{\sigma_x \varepsilon_x}{2}$$

Equation 10 - Strain energy density

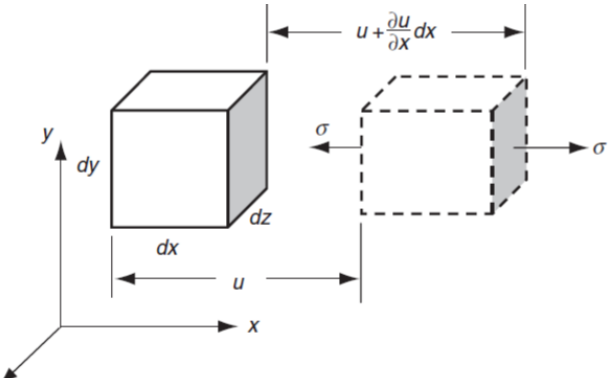

Figure 16 - Stress element with uniaxial stress [12]

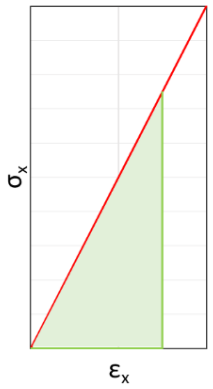

Figure 17 – Elastic stress-strain plot

The law of conservation of energy applies to strain energy. As a result, we can say that regardless of the sequence work is performed on a system the sum of work performed does not change. If we take the previous system and add loads along the Y- and Z-axes, the total work performed would simply be the sum of those individual loads and the result would be the strain energy equation for multiaxial loading shown in Equation 11. When simplified and using tensor index notation, and the Hooke's law equivalents are shown in Equation 12. The decomposition of strain energy, shown in Equation 13, into the sum of deviatoric and spherical stress and strain will be very useful when discussing failure theory. [12]

$$U = \frac{\sigma_x \varepsilon_x}{2} + \frac{\sigma_y \varepsilon_y}{2} + \frac{\sigma_z \varepsilon_z}{2} + \frac{\tau_{xy}^2}{2\mu} + \frac{\tau_{yz}^2}{2\mu} + \frac{\tau_{zx}^2}{2\mu}$$

Equation 11 - Multiaxial strain energy

$$U = \frac{\sigma_{ij}\varepsilon_{ij}}{2} = \frac{\lambda \varepsilon_{kk}\varepsilon_{jj}}{2} + \mu \varepsilon_{ij}\varepsilon_{ij} = -\frac{\nu}{2E}\sigma_{kk}\sigma_{jj} + \frac{1+\nu}{2E}\sigma_{ij}\sigma_{ij}$$

Equation 12 - Strain energy tensor notation

$$U = U_{spherical} + U_{deviatoric} = \frac{\hat{\sigma}_{ij}\hat{\varepsilon}_{ij}}{2} + \frac{\tilde{\sigma}_{ij}\tilde{\varepsilon}_{ij}}{2}$$

Equation 13 - Strain energy decomposition

Strain energy above yield stress takes on new characteristics. The definition of applied work remains the same, but stored energy is not fully recoverable. If we recall the Ramberg-Osgood method, Equation 14, we will see an elastic component based upon Hooke's law and a plastic component. Strain energy

applied to the elastic component is recoverable while the plastic component of strain causes permanent change in the solid material. The area under the Ramberg-Osgood curve is strain energy density as shown in Figure 18. [14]

$$\varepsilon^{total} = \frac{\sigma}{E} + \left(\frac{\sigma}{K'}\right)^{\frac{1}{n'}}$$

Equation 14 - Ramberg-Osgood

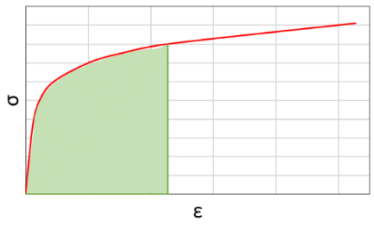

Figure 18 – Elastic-plastic stress-strain plot

Strain energy density has been applied to numerical methods and FEA models. The Neuber rule considers a structure that is generally subjected to stress below yield strength but highly localized stress concentrations with plastic deformation. In this case, large deformation theory is not required since plastic deformation does not dominate the response from the structure. Linear-elastic FEA material models are employed, and strain energy density is used as a transform between the elastic model and true plastic stress and strain. More accurate techniques are being developed including the modified Neuber rule and equivalent strain energy density method (ESED). The mathematical transform for monotonic loading from linear elastic FEA model stress (S) and strain (e) to true stress (σ) and strain (ε) is shown in Equation 15 and Equation 16 with a plot of equivalent strain energy in Figure 19. [13]

$$Se = \frac{S^2}{E} = \sigma\left(\varepsilon^{elastic} + \varepsilon^{plastic}\right) = \sigma\left(\frac{\sigma}{E} + \left(\frac{\sigma}{K'}\right)^{\frac{1}{n'}}\right)$$

Equation 15 - Modified Neuber rule

$$S = Ee = \sqrt{\sigma^2 + E\sigma\left(\frac{\sigma}{K'}\right)^{\frac{1}{n'}}}$$

Equation 16 – Equivalent strain energy

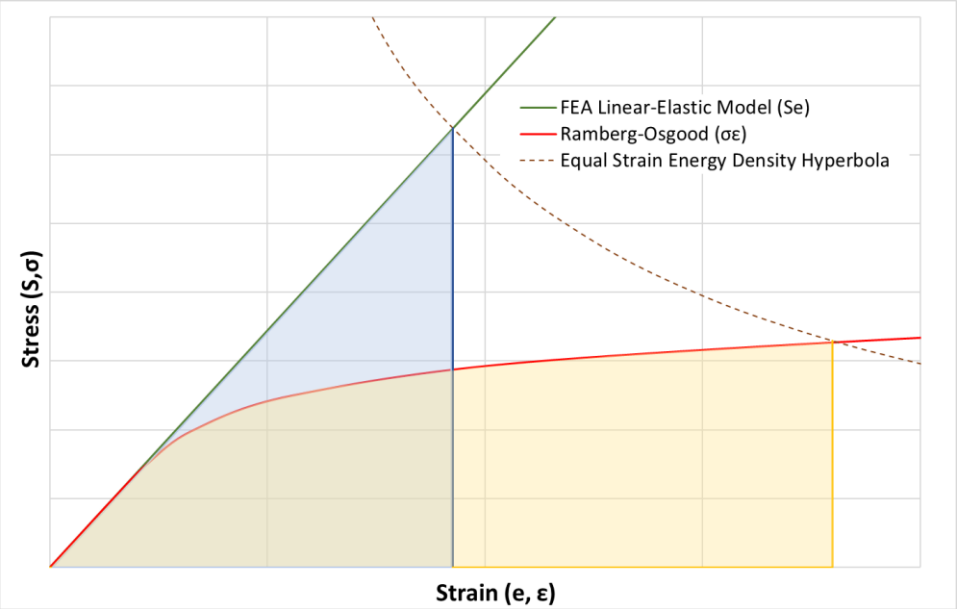

Figure 19 - Equivalent strain energy density - modified Neuber rule plot.

Cyclical loading and the hysteresis stress-strain curve for the stress concentration can also be created from the linear-elastic FEA results as shown in Figure 20. The loading history and hysteresis loops can be traced using Equation 17. The endpoint of each hysteresis loop becomes the starting point for the next loop. [13]

$$\frac{\Delta\varepsilon}{2} = \frac{\Delta\sigma}{2E} + \left(\frac{\Delta\sigma}{2K'}\right)^{\frac{1}{n'}}$$

Equation 17 - Ramberg-Osgood cyclic loading

$$\Delta e = \left[\frac{\Delta\sigma^2 + 2E\Delta\sigma\left(\frac{\Delta\sigma}{2K'}\right)^{\left(\frac{1}{n'}\right)}}{E^2}\right]^{1/2}$$

Equation 18 - Neuber correction for cyclic loading

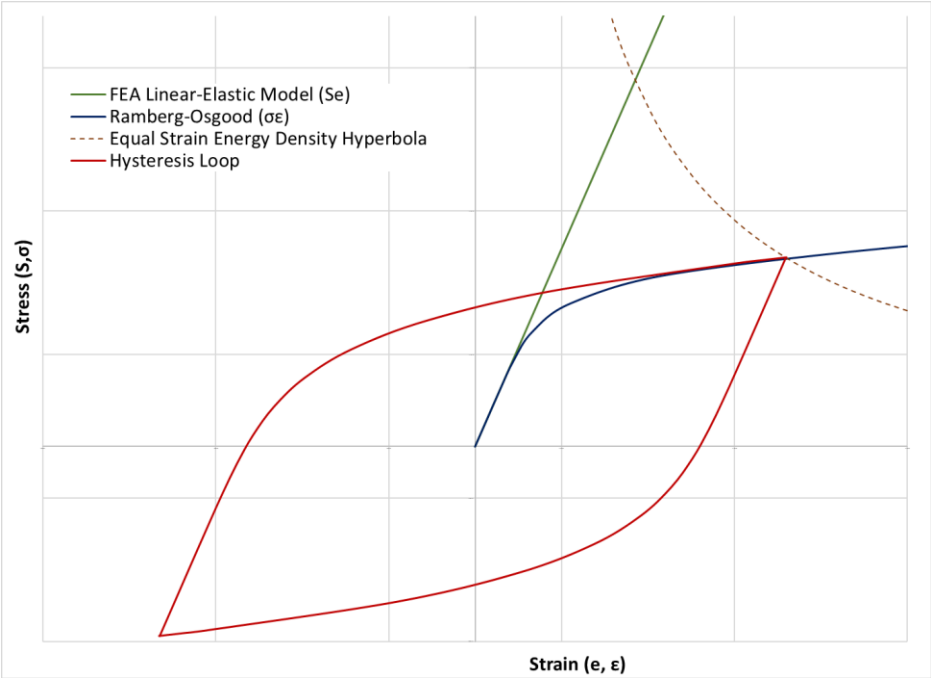

Figure 20 - Stress-strain hysteresis loop.

The values obtained from calculation of cyclic stress and strain will be used for fatigue-life estimation. Early scientific study of fatigue divided life estimations into two categories, stress-life or high cycle fatigue and strain-life also called low cycle fatigue. Let us introduce and discuss some of the most common methods. Basquin, building on previous study, proposed a power law relationship between stress-life and would plot life on a log scale as seen in Equation 19. Manson and Coffin independently proposed a similar power law relationship between strain-life shown in Equation 20. [15] The combination of stress-life and strain-life into a single equation unifies these two theories given the name Manson-Coffin-Basquin (MCB) shown in Equation 21. The influence from MCB and strain-energy can be seen in the method developed by Smith, Watson, and Topper (SWT) shown in Equation 22. [16] The variable and exponents found in Equations 18-21 are common to all and a strain-life plot is shown in Figure 21. Data for fatigue calculation is shown in Table 3. [17]

$$\frac{\Delta\sigma}{2} = \acute{\sigma}_f(2N_f)^b$$

Equation 19 - Basquin stress-life

$$\frac{\Delta\varepsilon}{2} = \acute{\varepsilon}_f(2N_f)^c$$

Equation 20 - Manson-Coffin strain-life

$$\frac{\Delta\varepsilon}{2} = \frac{\acute{\sigma}_f}{E}(2N_f)^b + \acute{\varepsilon}_f(2N_f)^c$$

Equation 21 - Manson-Coffin-Basquin life

$$\frac{\sigma_m\Delta\varepsilon}{2} = \frac{(\acute{\sigma}_f)^2}{E}(2N_f)^{2b} + \acute{\sigma}_f\acute{\varepsilon}_f(2N_f)^{b+c}$$

Equation 22 - Smith-Watson-Topper life

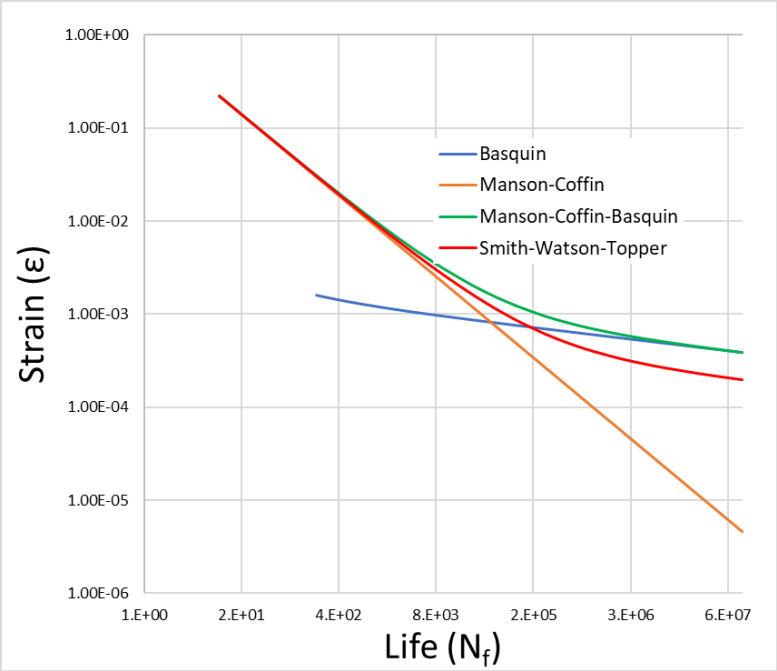

Figure 21 - Strain-life plot for 1100 aluminum.

Table 3 – Aluminum 1100 Fatigue Properties [17]

Property	Symbol	Value	Units
Young's Modulus	E	6.89E+10	Pa
Ultimate Tensile Strength	σ_u	1.17E+08	Pa
Yeild Strength	σ_y	3.70E+07	Pa
Cyclic strength coefficient	K'	1.546E+08	Pa
Fatigue strength coefficient	σ_f'	1.66E+08	Pa
Cyclic strain hardening exponent	n'	0.1437	--
Fatigue ductility coefficient	ε_f'	1.6433	--
Fatigue strength exponent	b	-0.0961	--
Fatigue ductility exponent	c	-0.6689	--

Fatigue failure and life calculation must be discussed using terminology from probability and statistics. However, the probability of failure, distribution of cycles to failure, and confidence interval remain a matter of speculation that could only be established through extensive physical experimentation. A minimum of 50 cycles has been specified and we can calculate a value for maximum stress, but that would be the median of the distribution for the number of cycles to failure. The result would be that our bell curve distribution will be centered on the minimum number of cycles and we would experience failure 50% of the time. A design or working curve is instead chosen to cover 95% of data distribution or estimated by eye. Estimation is a subjective method that lacks consistency but remains the only option available when data is unavailable. [18]

Ansys FEA software is divided into modules and each module requires a license. The fatigue module includes ESED correction for linear-elastic simulations with stress greater than yield strength for computing life. This module was not available for this project, so stress-strain results were collected and computation for Neuber correction and fatigue-life performed using Microsoft Excel.

Let us take a moment to evaluate the preceding information and discuss how to apply it to methods and assumptions. How will having differing alloy grades on opposite sides of the weld impact HAZ and strength? Recall the heat exchange pipe is 6061-T6 and the shield panel is 1100-H12 aluminum. The melting points and annealing temperatures are shown in Table 2 for reference. Adding 1100 aluminum to the weld metal mixture will dilute the alloying elements in the liquified metal. It is reasonable to assume this change in chemistry will result in some reduction in strength of the weld metal. The variability of the welding process makes computing the exact effect impossible.

Fermilab specifications require removal of some panels for servicing. The weld metal will be cut away, but the heat-affected zone of the base metal will remain. Welding to reattach the panel will occur

over the same surfaces. Will the HAZ metal be further annealed with each successive welding process? It seems to be a reasonable assumption that additional annealing will occur in both 1100 and 6061 aluminum with each successive weld. A minimum hardness or strength due to chemistry can also be assumed once the material has reached the fully annealed condition for each grade.

The conclusions from Malin's study are compelling. In all cases, the location of failure during tensile testing corresponded with the minimum microhardness measured. Microhardness is a corollary for ultimate tensile strength. The differences in ultimate tensile strength between 1100-O and 6061-O is roughly 11%. Recall from Figure 15 the difference between the hardness at the fusion line and the point of failure was 5%. The weld metal strength will also be a function of chemistry. 4043-O has the highest strength when compared to 6061-O and 1100-O. We will therefore use 1100-O aluminum as the basis for calculation of fatigue and cycle life.

An important assumption behind the elastic stress-strain computation is that the material is homogeneous and isotropic. Prior to welding, aluminum in the shield panels and heat exchange pipe are homogeneous. The reduced hardness in the HAZ results in non-homogeneous yield strength and ultimate strength. Young's modulus, however, remains constant. ESED methods assume that plastic deformation occurs only on highly localized stress concentrations and must not be used where the structure undergoes stress above yielding over broad areas. If yielding is confined within concentrated areas of the lower strength HAZ, then the assumptions supporting ESED will have been met. If maximum stress is concentrated only in areas of the lower strength HAZ, then the non-homogeneity of yield strength will become moot. The broader structure can then be considered homogeneous and isotropic.

3.4 Thermophysical Properties and Heat Transfer

Temperature changes and thermodynamics are what drive mechanical stress and strain in our system. Convection heat transfer between the aluminum heat exchange pipe and helium gas initiates the process and diffusion heat conduction carries heat from remote regions of the shield. Radiation and conduction from the exterior vacuum vessel then add heat energy to the cold shield.

Let us begin with the helium gas refrigerant. As the cooldown process begins, the incoming helium is room temperature, 296K. Incoming gas temperature decreases linearly at a rate of 20K per hour until the target temperature of 40K is reached. It takes some additional time for the entire system to reach a steady-state temperature. Helium remains a gas throughout the process but undergoes significant changes in specific heat (C_p), conductivity (λ), density (ρ), and viscosity (μ) with the temperature range of 296 to 40 Kelvin. Helium properties for the temperature range at a pressure of 800 kPa are listed in Table 4. [19] Several given and calculated values are included in the table as well. The given values are temperature (T) and heat exchange pipe inner diameter (d). The calculated values are average fluid velocity (ω), Reynold's number (Re), Prandtl number (Pr), Nusselt number (Nu), and convection coefficient (h). Values are computed for each temperature due to the change in properties. The convection coefficient will allow us to calculate the rate of convection heat transfer from the pipe to the helium fluid and will be the first equations we solve. A convection feature will be added to the FEA simulation and heat transfer computations will be processed within the FEA simulation. Mass flow rate ($\dot{m}$) has been estimated based upon the first law of thermodynamics using Equation 29. [20]

$$\omega = \dot{m}/(0.25\,\pi\,d^2\,\rho)$$ *Equation 23 - Helium average velocity*

$$\mathrm{Re} = \mathrm{d}\,\omega\,\rho/\mu$$ *Equation 24 - Reynold's number*

$$\mathrm{Pr} = \mu\,\mathrm{C_p}/\lambda$$ *Equation 25 - Prandtl number*

$$\mathrm{Nu_f} = 0.023\,\mathrm{Re_f^{0.8}}\,\mathrm{Pr_f^{0.4}}$$ *Equation 26 - Nusselt number*

$$\mathrm{h} = \lambda\,\mathrm{Nu/d}$$ *Equation 27 - Convection coefficient*

$$\dot{q}_{conv} = h\,A_s\,(T_f - T_s)$$ *Equation 28 - Convection rate*

$$\Delta U_{system} = U_{in} - U_{out} = \dot{q}_{in} - \dot{q}_{out} + W_{in} - W_{out} + U_{mass\,in} - U_{mass\,out}$$ *Equation 29 - Energy balance*

Table 4 - Properties of Helium at 800 kPa and Calculated Convection Heat Exchange Values

T(K)	ρ(kg/m^3)	C_p (J/(kg*K)	λ (W/(m*K))	μ (Pa*s)	d (m)	V (kg/s)	ω (m/s)	Re	Pr	Nu	h (W/(m^2*K))
30	12.59	5379	0.03518	4.801E-06	0.0381	**0.1**	6.966818	6.961E+05	0.73407	959.722	**886.169**
40	9.429	5293	0.0416	5.648E-06	0.0381	0.1	9.30239	5.917E+05	0.71863	835.606	**912.368**
50	7.551	5254	0.04766	6.414E-06	0.0381	0.1	11.61598	5.210E+05	0.70707	749.892	**938.054**
60	6.307	5232	0.05342	7.123E-06	0.0381	0.1	13.90712	4.692E+05	0.69763	685.861	**961.646**
80	4.746	5212	0.06426	8.425E-06	0.0381	0.1	18.4813	3.967E+05	0.68333	594.721	**1003.065**
100	3.807	5203	0.07439	9.630E-06	0.0381	0.1	23.03972	3.470E+05	0.67354	531.326	**1037.411**
120	3.178	5199	0.08396	1.077E-05	0.0381	0.1	27.59982	3.103E+05	0.66690	483.914	**1066.390**
140	2.728	5196	0.0931	1.187E-05	0.0381	0.1	32.15258	2.815E+05	0.66248	446.502	**1091.059**
160	2.39	5195	0.1019	1.295E-05	0.0381	0.1	36.69968	2.581E+05	0.66021	415.884	**1112.300**
180	2.126	5194	0.1103	1.399E-05	0.0381	0.1	41.25693	2.389E+05	0.65879	390.624	**1130.863**
200	1.915	5193	0.1185	1.505E-05	0.0381	0.1	45.80273	2.220E+05	0.65953	368.622	**1146.502**
220	1.742	5193	0.1265	1.608E-05	0.0381	0.1	50.35145	2.078E+05	0.66011	349.730	**1161.176**
240	1.597	5193	0.1343	1.708E-05	0.0381	0.1	54.92313	1.957E+05	0.66044	333.317	**1174.921**
260	1.475	5193	0.1418	1.805E-05	0.0381	0.1	59.46592	1.851E+05	0.66103	319.023	**1187.335**
280	1.37	5193	0.1492	1.901E-05	0.0381	0.1	64.02353	1.758E+05	0.66166	306.184	**1199.021**
300	1.279	5192	0.1565	1.994E-05	0.0381	0.1	68.57876	1.676E+05	0.66152	294.682	**1210.440**

Convection draws heat from the pipe's internal surface. Conduction carries heat by diffusion from the pipe through finger welds and from shield panels. Pipes, wires, and devices connect the exterior vacuum vessel and conduct heat to the intercept flange of the heat exchange pipe. The external connections to the heat exchange pipe have no influence on the temperature difference between the heat exchange pipe and shield panels. Many of the devices are complex and some lack CAD models. Fermilab engineers have performed heat conduction analysis and compiled the results in an engineering documentation report (ED0008200) shown in Table 6. Reinforced epoxy G10 support posts have been

included in the simulation and conduction will be computed. All other heat loads shown are less than 6% of total heat transfer during transient cooldown and will be applied to the FEA model as constant loads. Planning and budgeting for total cryogenic requirements has been provided in Fermilab engineering documentation (ED0009659) shown in Table 5 for reference only.

Table 6 - Computed Heat Loads per Device for HB650 (ED0008200)

	Each unit (W)			#	Total (W)		
	35-50 K	5 K	2 K		35-50 K	5 K	2 K
Cavity dynamic load			19.20	6			115.2
Input coupler (static)	1.10	0.04	0.56	6	6.6	0.2	3.4
Input coupler (dynamic)	7.50	2.20	0.54	6	45.0	13.2	3.2
Support post	2.18	0.40	0.18	12	26.2	4.8	2.1
Beam line		0.73	0.29	2	0.0	1.5	0.6
Thermal shield	61.33		1.86	1	61.3		1.9
View ports	0.24		0.71	4	0.9		2.8
Relief line	1.13		0.52	1	1.1		0.5
Valves & instrumentation	7.59	2.00	0.60	-	7.6	2.0	0.6

	35-50 K	5 K	2 K
Total static	103.8	8.6	11.9
Total dynamic	45.0	13.2	118.4
Total static + dynamic	148.8	21.8	130.3

Table 5 - Total Cryogenic Power Budget for HB650 (ED0008200)

Maximum allowed heat load to 50 K, W	**255**
Maximum allowed heat load to 5 K, W	45
Maximum allowed heat load to 2 K, W	175

Material thermodynamic properties of shield panels, pipes, and support posts change with temperature. Figure 22 shows a plot of specific heat values for a variety of materials. Figure 23 shows a plot of thermal conductivity and temperature and Figure 24 shows temperature effects on thermal strain. Data for specific materials can be found through the National Institute of Standards and Technology and their cryogenic material properties database. [21] Tabulated values have been incorporated into Ansys engineering data for each material.

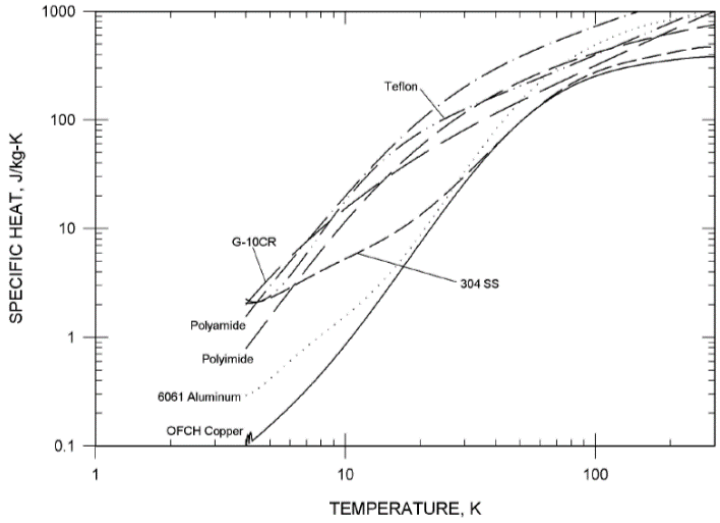

Figure 22 - Specific heat changes due to temperature for selected solids. [21]

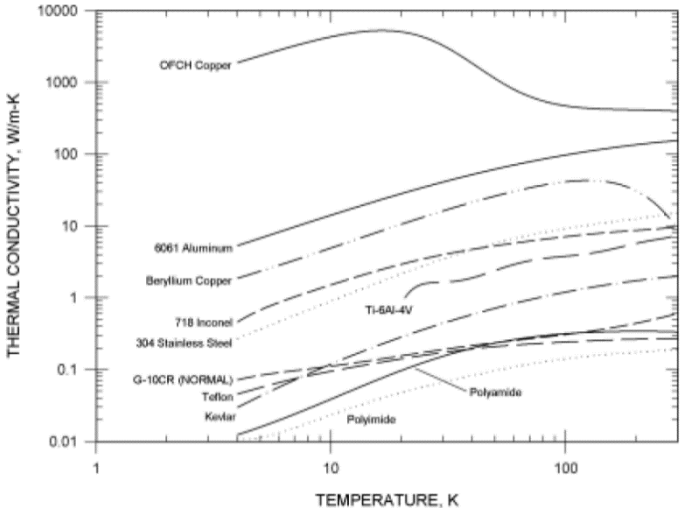

Figure 23 - Thermal conductivity changes due to temperature for selected solids. [21]

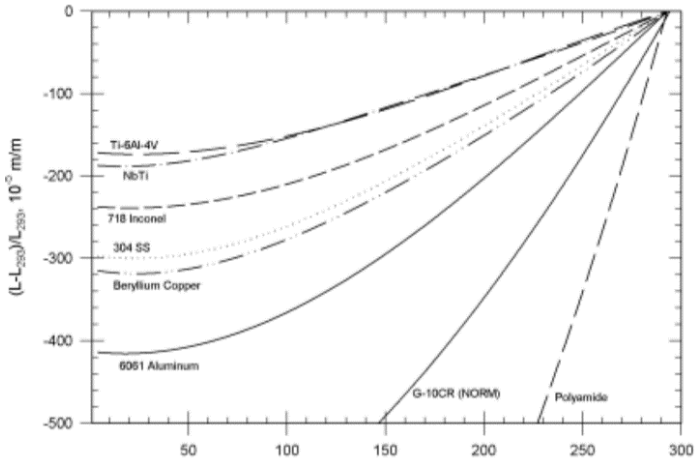

Figure 24 - Thermal strain changes due to temperature for selected solids. [21]

Convection draws heat from the pipe's internal surface, reducing surface temperature. Conduction carries heat by diffusion from the pipe through finger welds and from shield panels. Joseph Fourier, a French physicist and mathematician, stated:

> When heat is unequally distributed among the different parts of a solid mass, it tends to attain equilibrium, and passes slowly from the parts which are more heated to those which are less; and at the same time it is dissipated at the surface, and lost in the medium or in the void. The tendency to uniform distribution and the spontaneous emission which acts at the surface of bodies, change continually the temperature at their different points. [22]

Fourier's law of heat conduction and the analytical methods developed in the 19th century remain the fundamental understanding in the 21st century. The assumptions for Fourier's equation include having an isotropic, homogeneous, solid body with constant density, specific heat, and thermal conductivity. As previously discussed, specific heat and thermal conductivity vary with temperature. Likewise, analytical solution is only possible if the solid body has a simple shape where geometry can be expressed with differential equations. FEA numerical methods divide or discretize geometry into simple shapes and discretize time into short periods where material properties can be considered constants. The purpose of FEA transient thermal simulation is finding the solution for Equation 30 and the temperature distribution at each point and time in the solid body or structure.

$$\nabla^2 T(r,t) = \frac{\rho C_p}{k} \frac{\partial T(r,t)}{\partial t}$$

Equation 30 – Fourier equation

Heat transfer through radiation depends on the temperature (T) of each surface, the area exposed (A) and the emissivity (ϵ) of each surface. Multilayer insulation (MLI) has little resistance to convection or conduction. The principal purpose of MLI is to obstruct radiation. Each MLI layer receives most of the heat from the outer surface and emits half of the heat it receives from both its inner and outer surfaces. The difference between the radius of the inner surface of the vacuum vessel, each consecutive layer of

MLI, and the outer surface of the thermal shield is negligible. Computation has been simplified by lumping curved cylindrical surfaces with the flat end panels. The radiation heat transfer formula for two flat and parallel surfaces is shown in Equation 31. [20] Rather than create model geometry for thirty layers of MLI, the radiation insulation values have been combined and a single emissivity value of 0.003276 applied to the surfaces of the thermal shield. Radiation heat transfer is then computed through transient thermal FEA analysis.

$$\dot{q} = \frac{A(5.7 * 10^{-8})(T_h^4 - T_c^4)}{\frac{1}{\epsilon_h} + \frac{1}{\epsilon_c} - 1}$$

Equation 31 - Radiant heat transfer

3.5 SSR1 Updated Analysis

A Fermilab engineering specification document, ED0006891, describes the analysis performed of the SSR1 thermal shielding and conclusions reached. Figure 25 gleaned from that report shows a cross-sectional view looking down the beam pipe through the SRF cavities. [6]

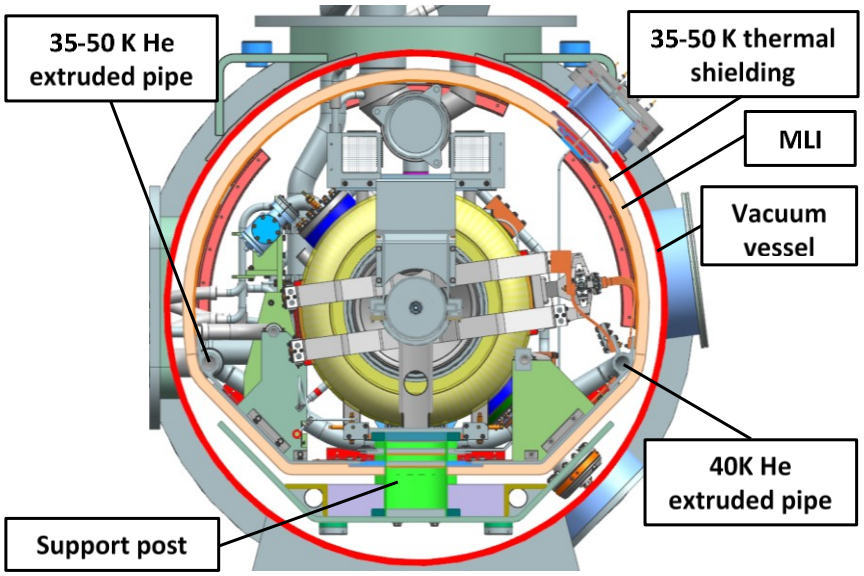

Figure 25 - SSR1 cryomodule axial section view.

Also from ED0006891, Figure 26 displays the time step during cooldown where equivalent stress peaks with a 5 Kelvin per hour cooling rate and Figure 27 with a 10K/hr cooling rate. [6] Has the assumption been met and is plastic deformation limited to highly localized stress concentrations? From Table 2 we are looking for four yield stress values. 1100 aluminum might be as low as 34.5 MPa if the material is fully annealed or 117 MPa further from the weld. 6061 aluminum could be as low as 48.3 MPa in the annealed condition or as high as 276 MPa in the T6 condition. We can see this more clearly if the scale is reset to differentiate between the yield strength values of interest as seen in Figure 28. The scale and inset image are shown in Figure 29.

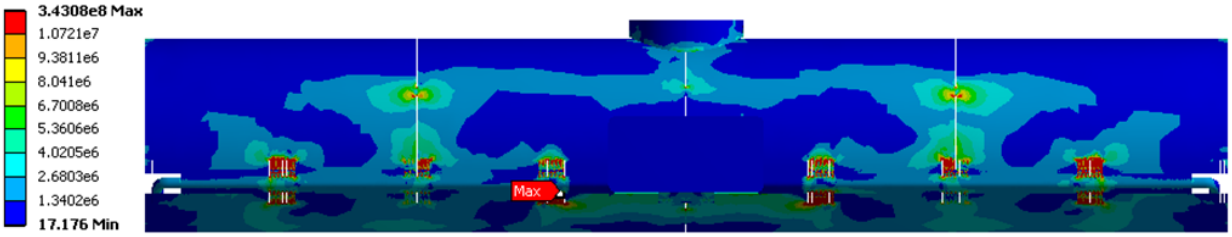

Figure 26 - SSR1 5K/hr cooldown maximum stress (ED0006891)

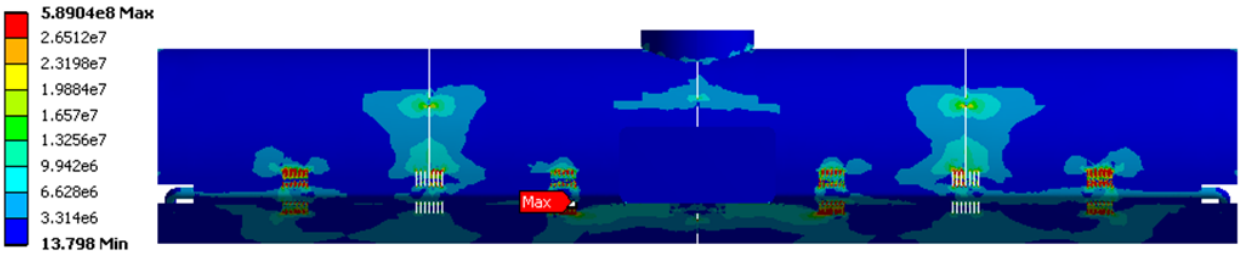

Figure 27 - SSR1 10K/hr cooldown maximum stress (ED0006891)

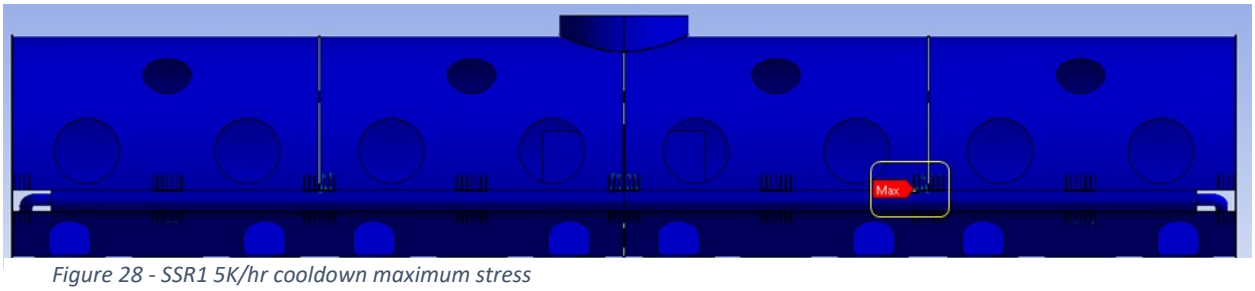

Figure 28 - SSR1 5K/hr cooldown maximum stress

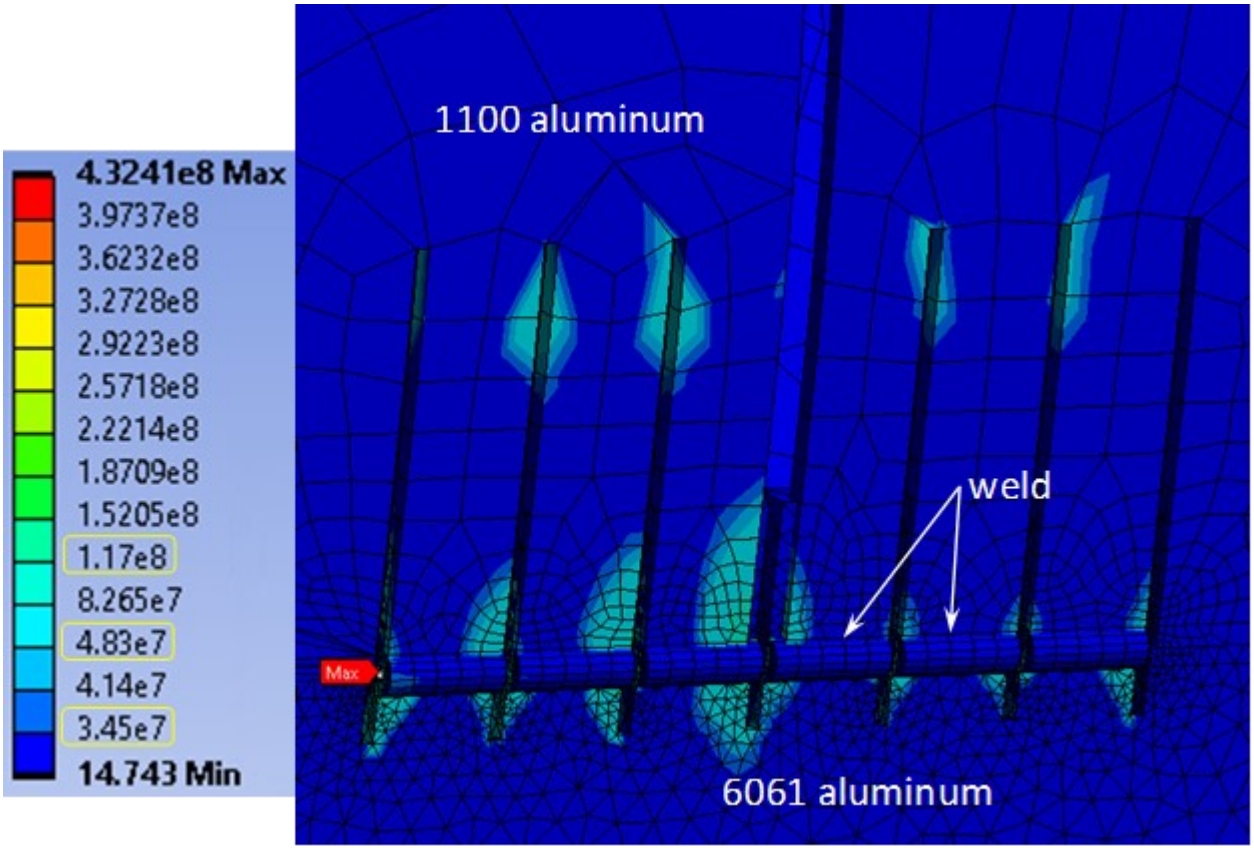

Figure 29 - SSR1 finger joint close-up. Maximum stress at 5K/hr

The scale in Figure 29 has three of the yield strengths of interest circled in yellow. In Figure 28 the only locations where stress is above 34.5 MPa are at the finger joints. A closed look at Figure 29 shows elevated stress at the top of the slots. These stress concentrations are further than 25 mm from the welds and are therefore outside the HAZ. The expected yield strength for 1100 aluminum in these locations is 117MPa and the peak values are slightly lower. Although not critical in the current stress state, sharp re-entrant corners at the top of the slots could be causing stress concentrations, so a new feature will be added during redesign to alleviate this condition. Near to the welds there are concentrated areas of stress above yield strength. This is however no ordinary stress concentration. A mathematical anomaly in an FEA model is present which artificially inflates the peak value called a singularity. As mesh is refined stress increases without limit rather than converge on a value.

One method for convergence study is to plot stress along a path that intersects the singular point. Refinement of the mesh and plotting stress along the path shows a nearby point that does converge. Figure 32, Figure 31, and Figure 30 show a path with varying mesh size. In Figure 33 we observe stress values begin to converge between 0.20 and 0.25 mm away from the singular point giving an approximate peak stress of 350 MPa. Neuber correction gives 87.5 MPa true stress and a median 390 MCB cycles of life.

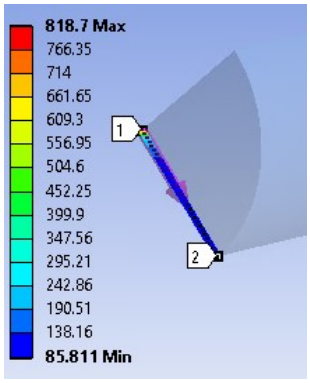

Figure 32 – Convergence fine mesh

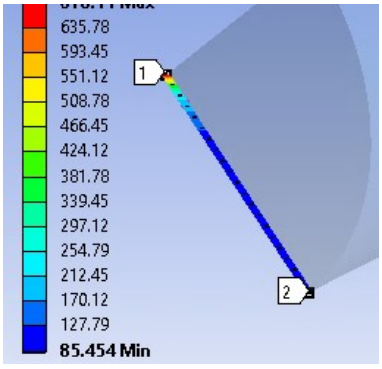

Figure 31 – Convergence medium mesh

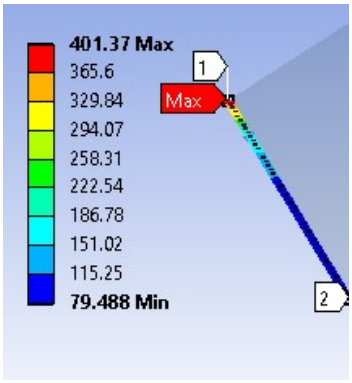

Figure 30 – Convergence coarse mesh

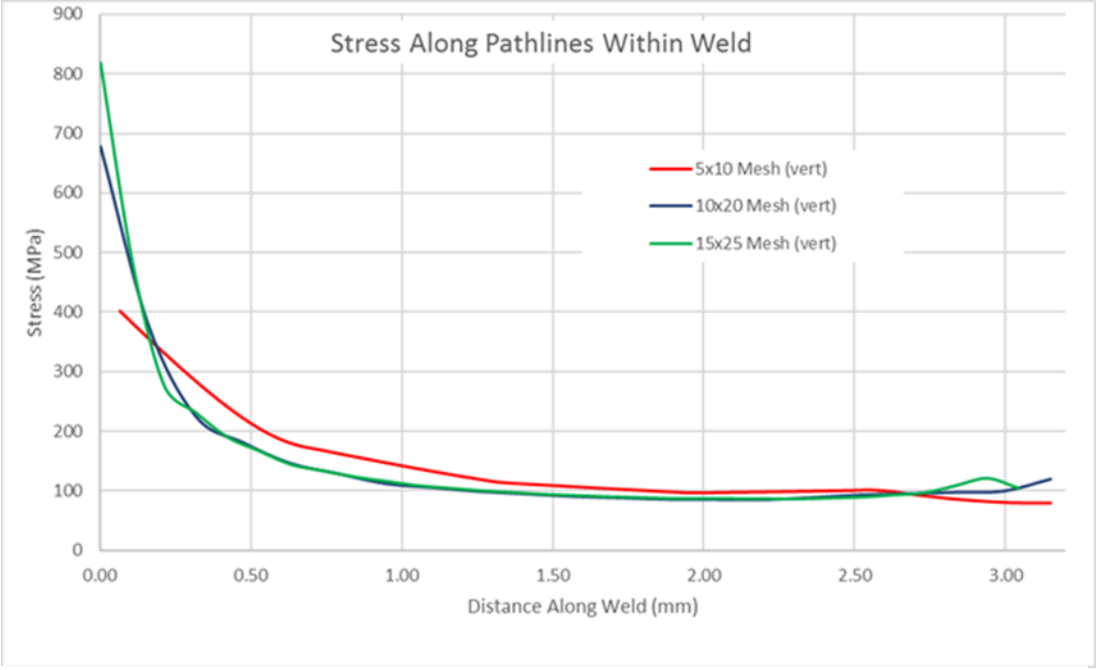

Figure 33 - Convergence study plot

Thermal strain is the principal source of stress with gravity body forces contributing minimal amounts. Structural members are welded at room temperature when the lengths are equal, and stress is minimal. Thermal strain is a change in volume per unit temperature. With an isotropic material the change is equal in all directions, so we can equate this to a change in length per unit temperature. The greater the change in temperature, the more change in length. The difference in temperatures between finger welds indicated by the red oval in Figure 34 provides the greatest contribution to stress. Reviewing the temperature map in this critical region we see a difference of 26K while the distance between finger welds varies from 650 to 720mm.

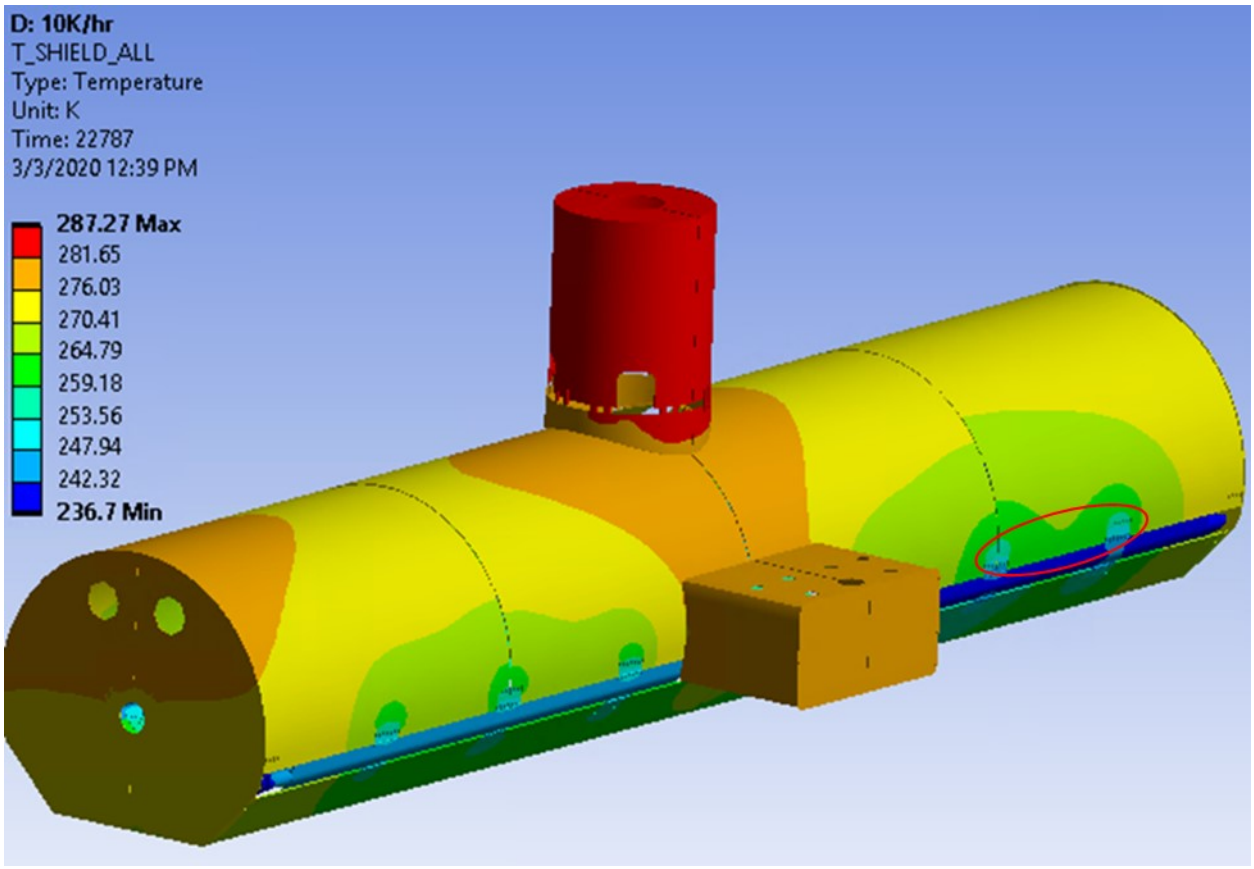

Figure 34 - Temperature distribution map of SSR1 at the moment of greatest stress (5K/hr)

Changing the panel material to copper would improve thermal conductivity and decrease the thermal gradient. This option was beyond the limited scope permitted. Currently there are six fingers side by side. Equally spacing the same number of fingers along the length of the panel would have an impact on peak temperature within the critical region. The goal of changing the cooling rate involves removing the same amount of heat energy from the system over a shorter time. The necessary increase in heat flux shown in Equation 32 involves either a greater temperature gradient $(T_h - T_c)$ or increased cross-sectional area (A_c) since material conductivity (k) is constant. Increasing the temperature gradient would increase stress. The bottleneck or smallest cross-sectional area heat must pass through is the weld.

$$\dot{q} = kA_c(T_h - T_c)$$ *Equation 32 – Convection heat flux*

The top panels on PIP-II cryomodules will be field welded after the cold mass is fully assembled. The bottom edge of the top panel will be welded to the flange face of the heat exchange pipe. Gravity will tend to pull the liquid weld metal bead away from the root increasing difficulty and potentially reducing weld quality. Changing weld orientation to vertical would mitigate this risk. Increasing the cross-sectional area of the weld without increasing the width of the finger would simply change the location of the bottleneck.

Several designs were evaluated using small scale FEA simulations. Variations in spacing, length of weld, alternative geometry, length of slot, and thickness of material were tested. Prototypes of the two finalists were produced. The first modified weld joint proposed was a single, vertical slot weld. The advantage offered by this weld was to connect two edges of the shield panel instead of just one as compared with the previous filet weld. Doubling the cross-sectional area for the same length of weld would increase heat flux. Holes were added to the ends of the slots to mitigate stress concentrations due to re-entrant corners. A prototype was created for evaluation by Fermilab technicians and a photo

of the results is shown in Figure 35. Unfortunately, this option was rejected by Fermilab technicians who had previously never produced slot welds. An alternative was to increase the width of the slot to accommodate two filet welds as shown in Figure 36. Heat flux was equivalent, but the workload and total length of weld was doubled. A proposal drawing for the new geometry is shown in Figure 37.

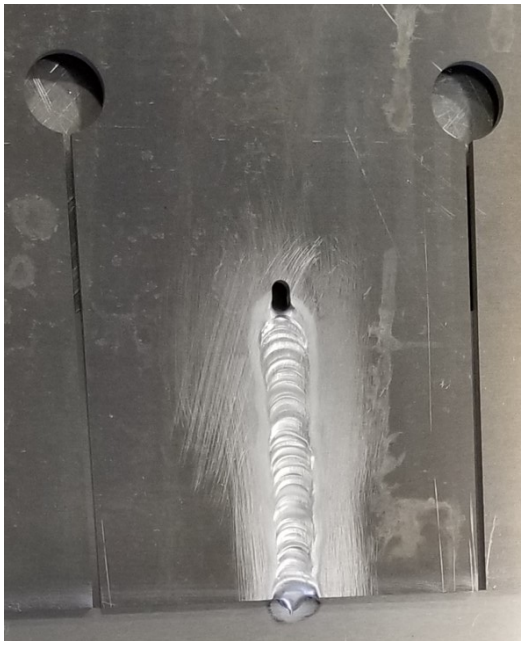

Figure 35 - Prototype slot weld sample

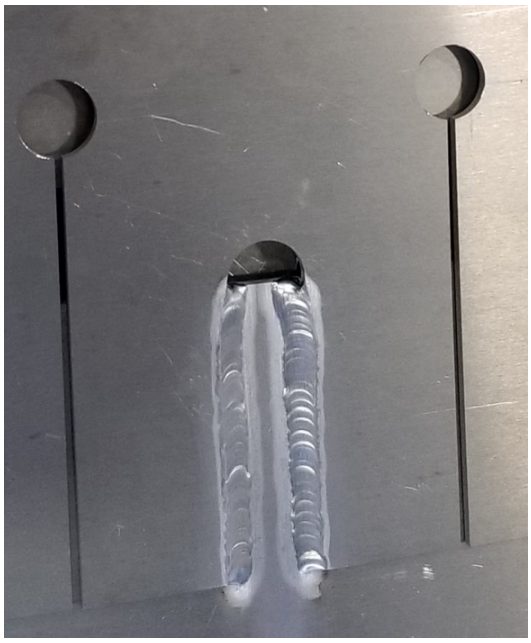

Figure 36 - Prototype fillet weld sample

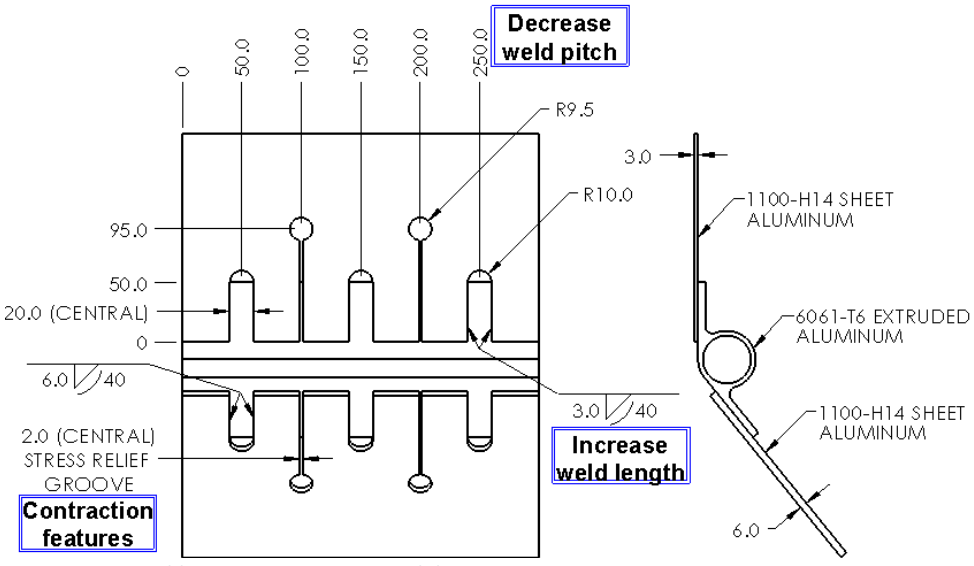

Figure 37 - Weld joint geometry proposal drawing

The wide groove with two fillet welds was selected for design and geometry for the thermal shield was created using Siemens NX computer aided design (CAD) software. This model was then imported into ANSYS Workbench for full scale computational analysis. As we will see in the results section, this design was capable of 40K/hr while maximum stress was less than SSR1 at 5K/hr. These results far exceeded expectations of the Fermilab engineering team and managers except for the amount of additional welding. The decision was made to compromise and weld just one side of the slot. We will see in the results section that the system was still capable to meet the expected 20K/hr with nearly the same number of welds to a comparably sized LCLS-II cryomodule thermal shield.

3.6 Model and Mesh Creation

With both NX and Ansys installed on the same workstation additional features in each software are available in each including the option to transfer currently visible CAD model geometry directly into Ansys. There is no permanent link back to NX from the imported geometry in Ansys and modifications can be made using any of the available tools within Ansys, Space Claim, or Design Modeler. The imported geometry meshed with Ansys automatic settings produced poor results shown in Figure 39. The majority of time would be spent modifying the geometry, mesh and contact refinement. Space Claim is a module of Ansys for creating and modifying model geometry. Removing unwanted features like fastener holes and beveled edges for weld preparation was relatively easy. Being able to refine the mesh for more accurate and detailed analysis in critical areas was the most important reason for manipulating geometry. Ansys has several tools for meshing bodies, but some bodies are too complex to be meshed with those tools. Dividing bodies can produce two or more new bodies that are easily meshed for better results. It should also be noted that there is a memory limit and each node and element require memory space. More nodes and elements also require more processor time for solution. Refined mesh for areas of interest and coarse mesh everywhere possible. For the HB650, the

welds and surrounding area is the focus of study. As seen in Figure 38, the model was divided into multibody parts to accomplish the discretization goals.

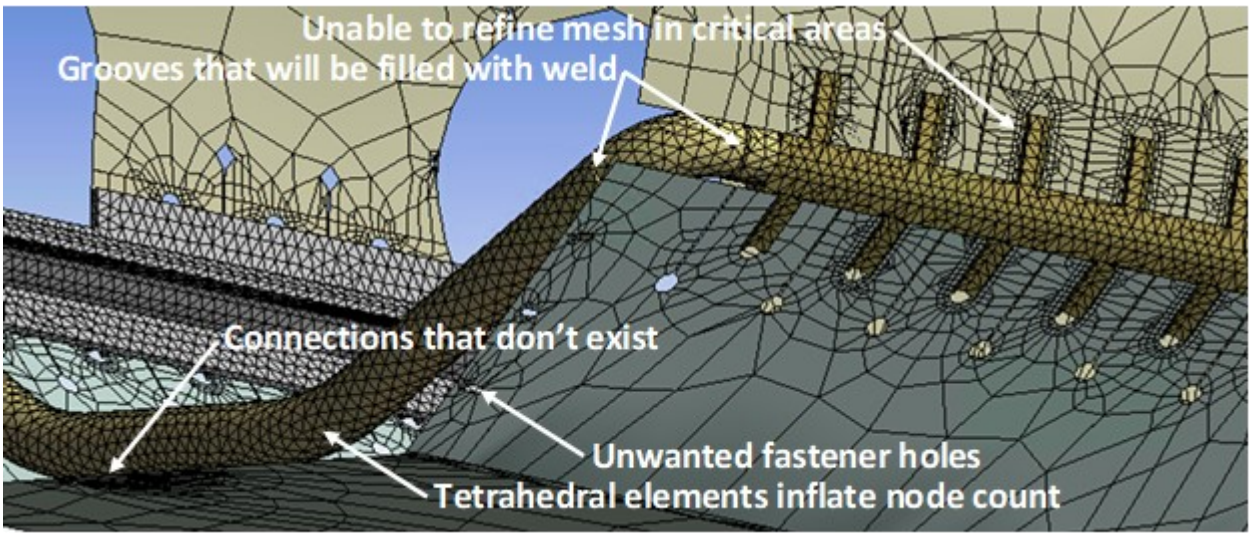

Figure 39 – Initial Ansys meshing results

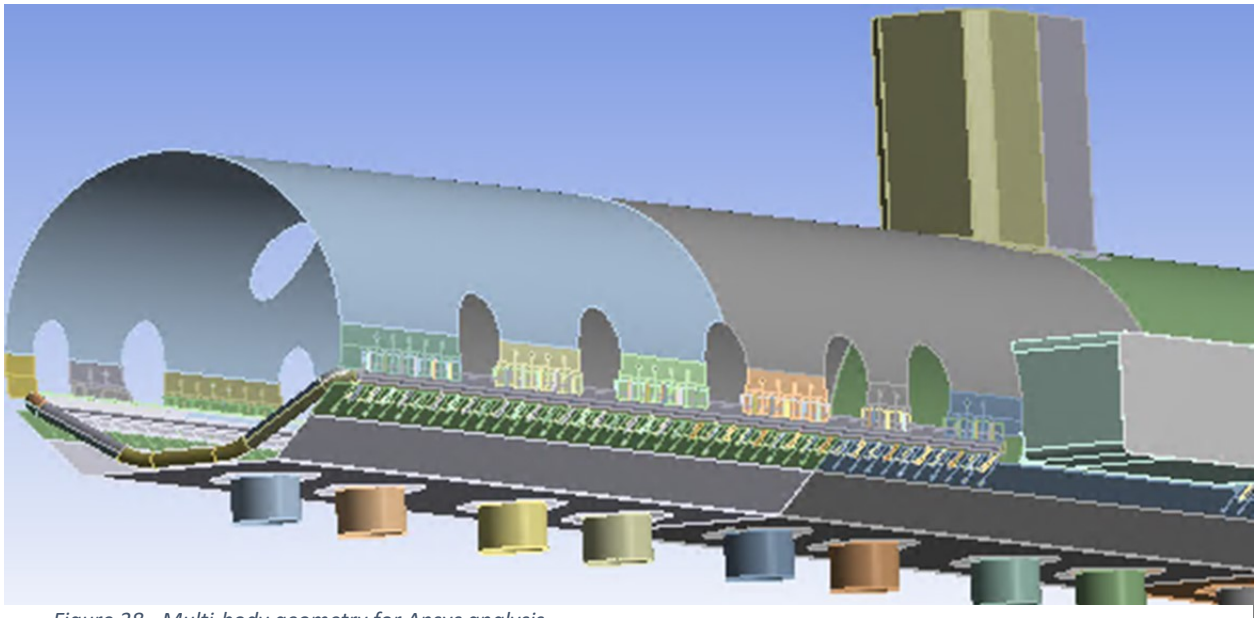

Figure 38 - Multi-body geometry for Ansys analysis

Having divided the bodies, the next step was stitching them back together. Two broad options are available in the software. The first is to create contacts within Ansys Workbench and the other is to create shared topology features within Space Claim. Shared topology matches surfaces or edges of both bodies. When mesh is created in Ansys, nodes for one body will be reproduced identically on the next body for the matched edges or surfaces. The shield panels in Figure 40 are surface bodies with the edges outlined in red. Blue edges are shared topology connecting the bottom parts of the panel with the top. The heat exchange pipe components are solid bodies and the magenta edges the outline of shared faces. Teal shared faces are visible in the close-up of Figure 41.

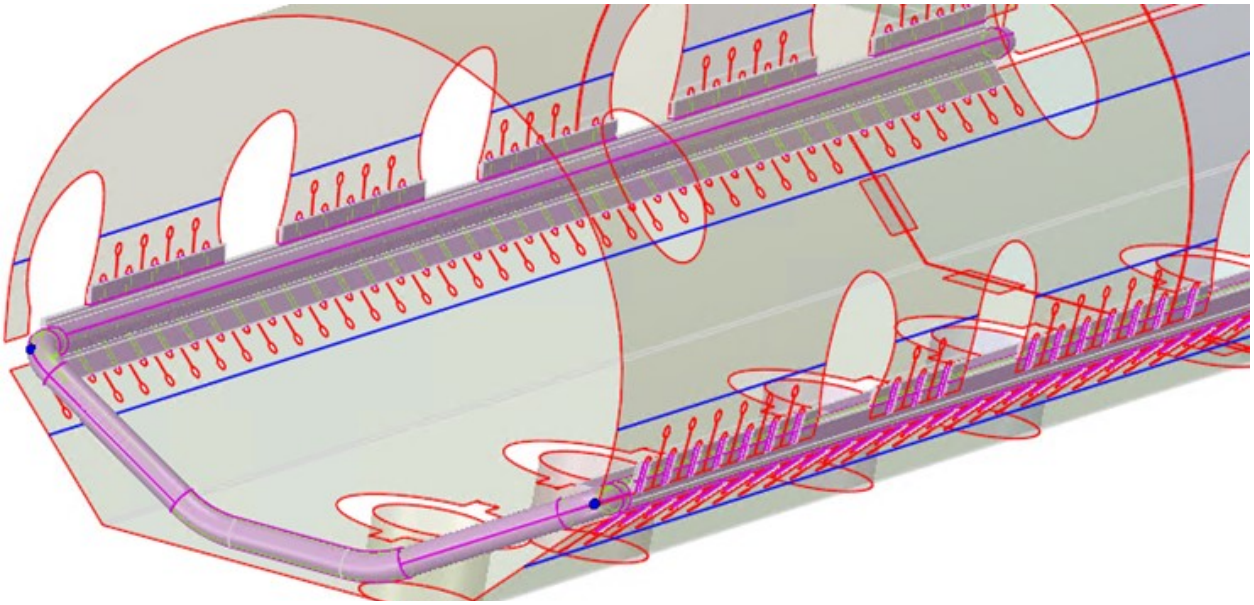

Figure 40 - Shared topology created in Space Claim

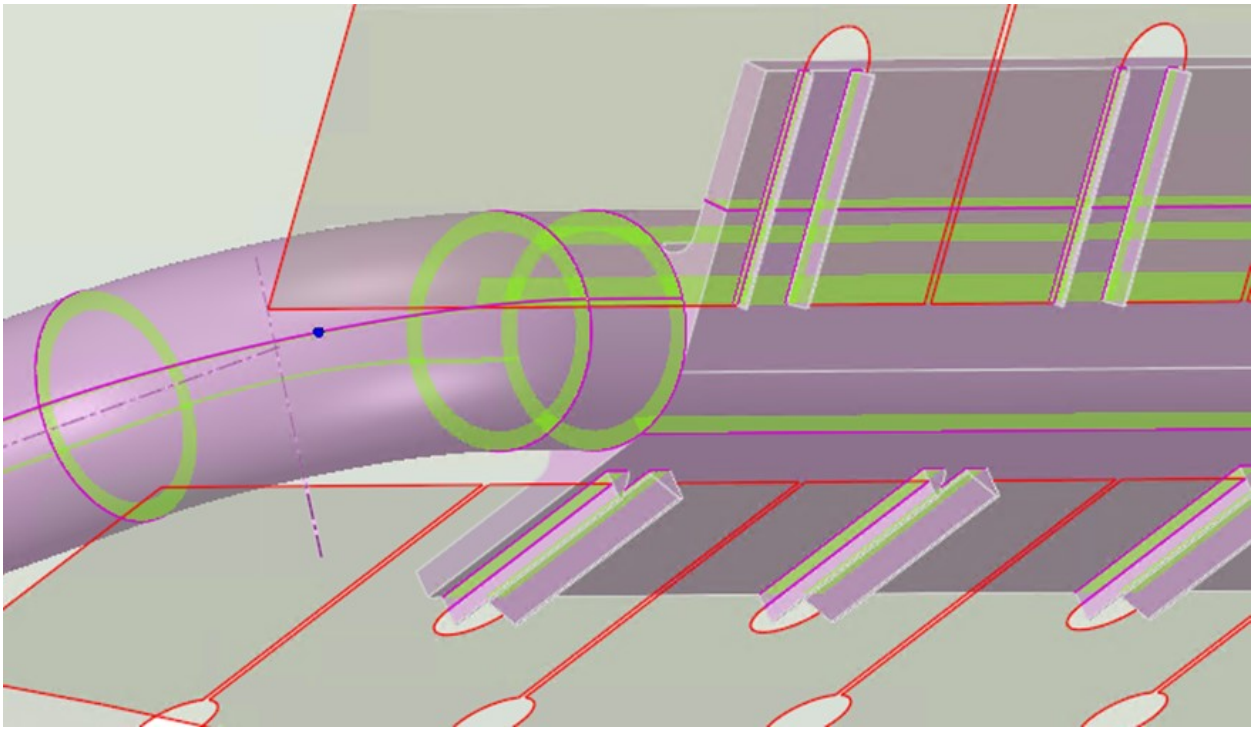

Figure 41 - Shared topology created in Space Claim close-up

Mesh size and type for a body or face can be specified. Multibody structural members can have multiple mesh sizes and types and be refined in an area of interest and coarse in others. For the HB650, the welds and surrounding area is the focus of study and are the finest mesh in the model. When weld bodies are meshed before others, shared topology will copy the refined mesh to the adjacent body. Similar bodies are grouped using named selection and the mesh sequence automated through the mesh worksheet shown in Figure 42.

Worksheet

Mesh

Generate Mesh | Start Recording

Clear Generated Mesh | Delete All Steps

√	Step	Named Selection
☑	1	Helium
☑	2	Mesh 10
☑	3	Mesh 0
☑	4	Mesh 7
☑	5	Mesh 1
☑	6	Mesh 2
☑	7	Mesh 3
☑	8	Mesh 4
☑	9	Mesh 5
☑	10	Mesh 6
☑	11	Mesh 8
☑	12	Mesh 9
☑	13	Mesh 11
☑	14	Mesh 12

Figure 42 - Ansys mesh worksheet

If the fine mesh bodies are first in sequence, the resulting mesh gradually increases as the next body in sequence is meshed. The HB650 welds are shown close-up in Figure 43 and another view of the larger structure is shown in Figure 44. This meshing scheme provided accurate results in the areas of interest while budgeting memory and processor time for the overall analysis.

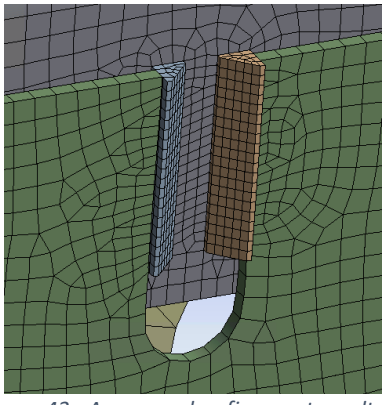

Figure 43 - Ansys mesh refinement results close-up

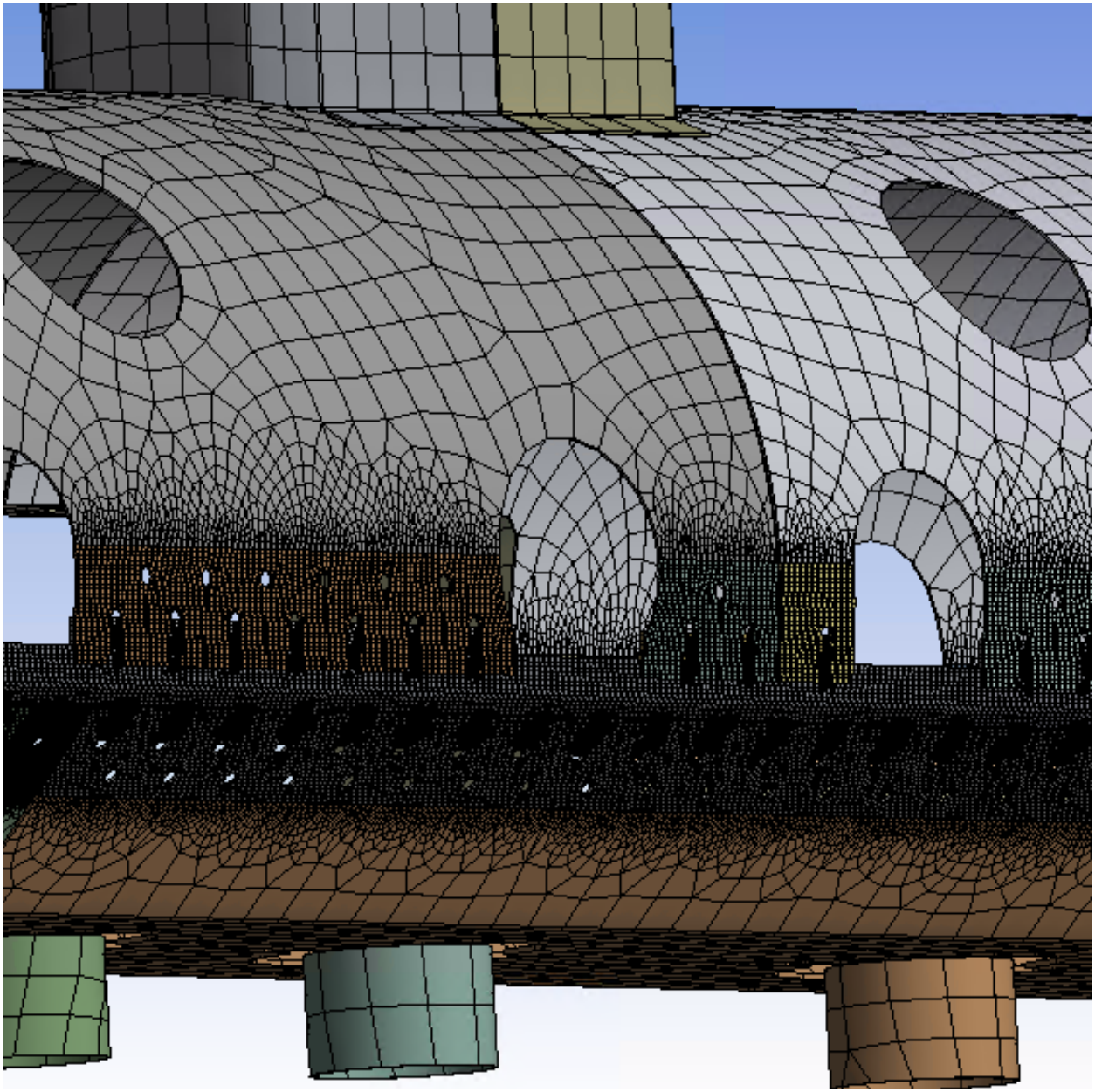

Figure 44 - Ansys mesh refinement results

3.7 Steady State Thermal Boundary Conditions

There are two boundary conditions that calculate the heat load from the environment and the remainder are simple, constant heat loads. Heat loads arising from conduction through the G10 support posts and radiated heat from the vacuum vessel are computed within the FEA model. The conduction heat loads from pipes, wires, and devices were not simulated but applied as simple constant heat sources and the values obtained from ED0008200 and shown in Table 6. The location where copper thermal conductors are connected is identified for each of these devices. Radiant heat load is applied to all exterior surfaces.

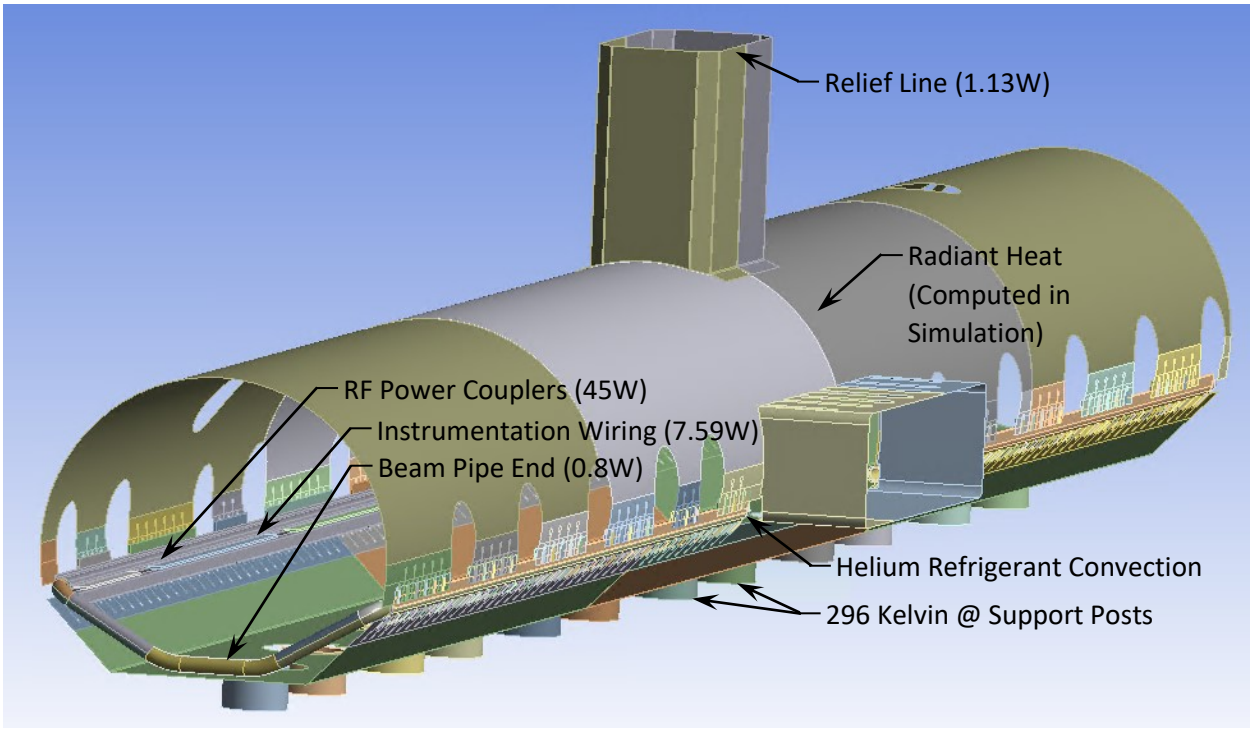

Figure 45 - Steady state heat loads and their locations

3.8 Transient Thermal Boundary Conditions

The heat loads for transient thermal simulation are like those found in steady state thermal simulation with differing values. During the cooldown time, the cryomodule is not active and most devices are not drawing electrical or RF power. Small monitoring devices and sensors draw little power and ohmic heating is negligible. With RF power not flowing through the couplers, there is a significant reduction in the heat load.

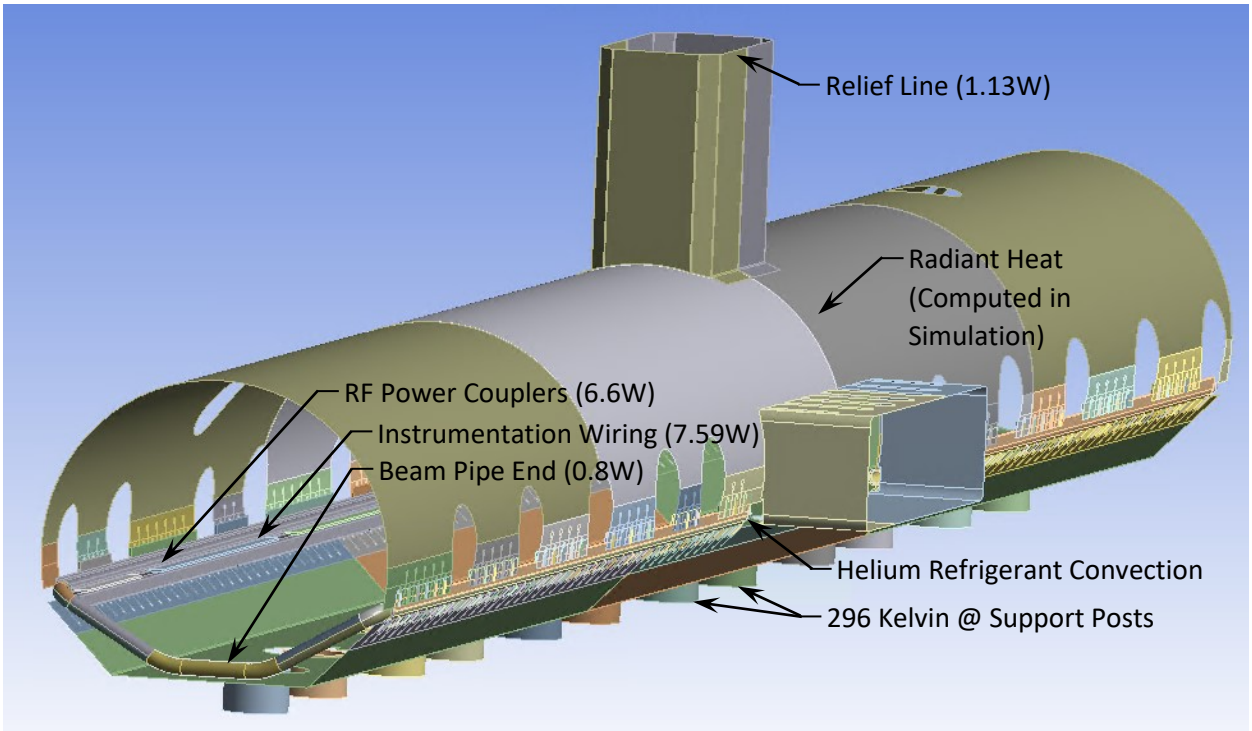

Figure 46 – Transient thermal heat loads and their locations

3.9 Structural Boundary Conditions

Boundary conditions for the model mimic real-life conditions and connections while leaving the structure free to contract due to cooling. All support posts are fixed at the edge of the base since that edge is kept at a constant 296K and no shrinking occurs. The platform epoxied to the top of the support post is not included in the model, so the top edge of the support post is coupled to the inner diameter edge of the lower shield to allow energy to pass between the two edges. Each of the lower shield inner diameter edges normally supported by the platform are fixed only in the Z direction, but are free to move in X and Y. A point on the lower shield near to the center is fixed in X and Y to prevent movement of the structure during simulation. Another point near the end of the lower shield prevents rotation of the structure by preventing movement in the X direction. Earth gravity is applied to the body in the negative Z direction.

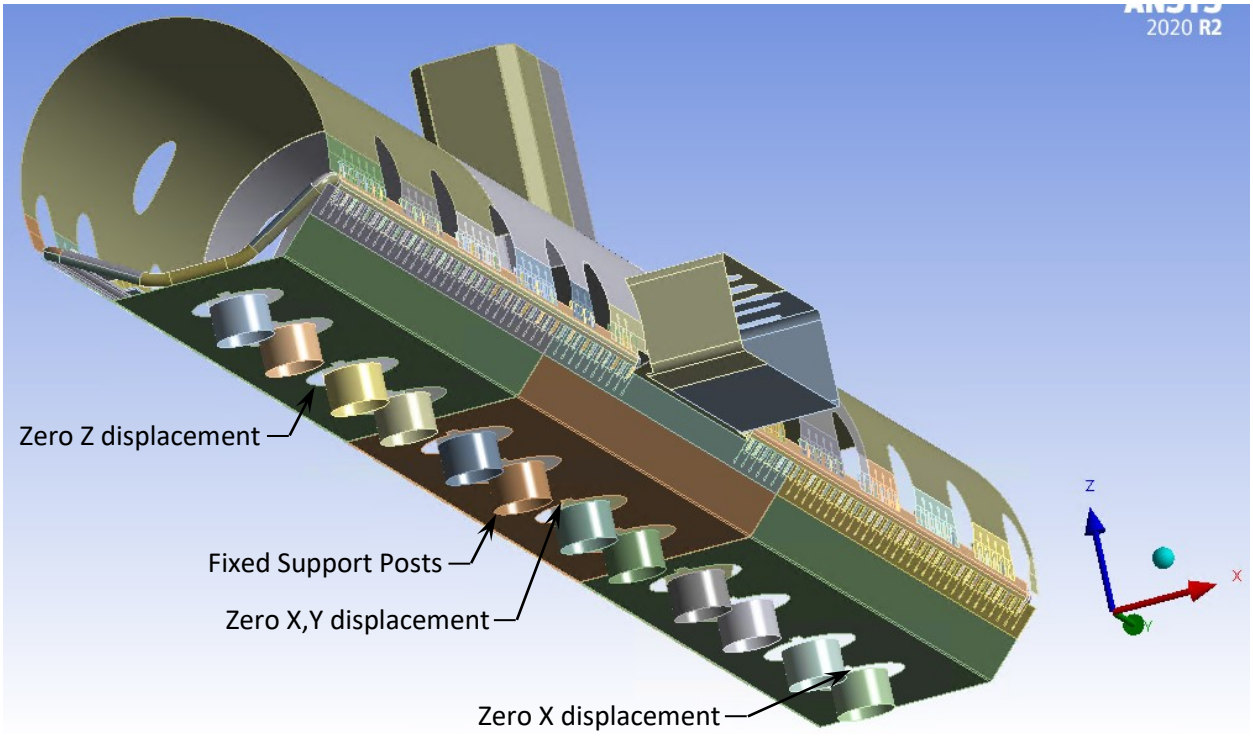

Figure 47 - Structural boundary conditions

Chapter 4: Results

4.1 Results Introduction

In this chapter the results of analysis and calculation will be presented along with a conclusion and future work discussion. Steady state thermal simulation results will be compared with specifications and cryogenic power budget. Transient thermal results or temperature map for the moment corresponding to peak stress. Structural analysis results showing maximum stress for the optimal design will be presented with calculation of the transformed true stress and predicted cycles of life. Structural analysis for the implemented design will also be review. Simulated maximum stress will be transformed to true stress and cycles of life predicted.

4.2 Steady State Thermal

The purpose of steady state thermal analysis is to confirm the thermal power budget provided by ED0008200 shown in Table 7 is not exceeded and temperatures anywhere on the shield fall between 35 and 50 Kelvin. Only results for the final design selected will be presented since all results for other designs are similar. The method used to measure thermal power in the steady state thermal simulation is to measure the temperature change in helium gas refrigerant and compute power using Equation 33. Thermal power calculated using this formula is 101.20 Watts $\left(\dot{m} = \frac{0.08\ kg}{s};\ C_p = \frac{5293 J}{kg\ K}\right)$. The temperature distribution over the thermal shield is shown in Figure 49. All specifications have been met.

$$\dot{q} = \dot{m}\ C_p\ (T_{out} - T_{in})$$

Equation 33 - Thermal Power

Table 7 - Total cryogenic power budget for HB650 (ED0008200)

Maximum allowed heat load to 50 K, W	**255**
Maximum allowed heat load to 5 K, W	45
Maximum allowed heat load to 2 K, W	175

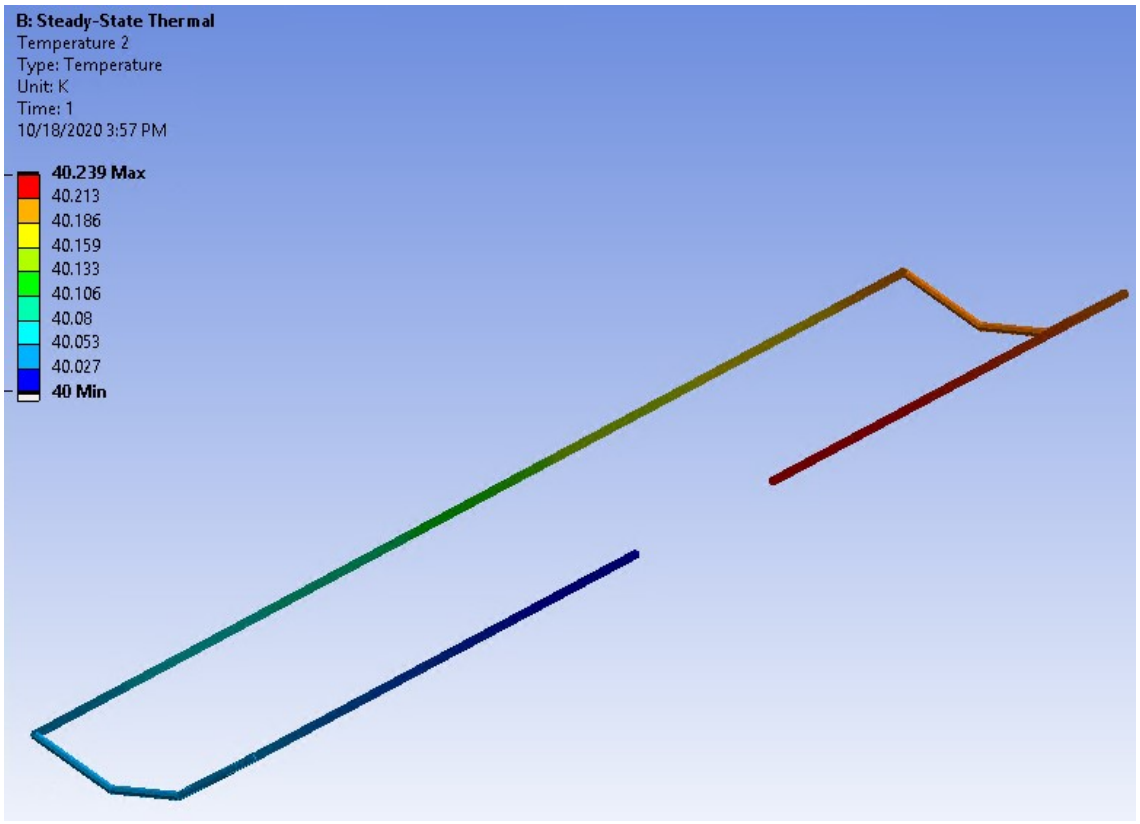

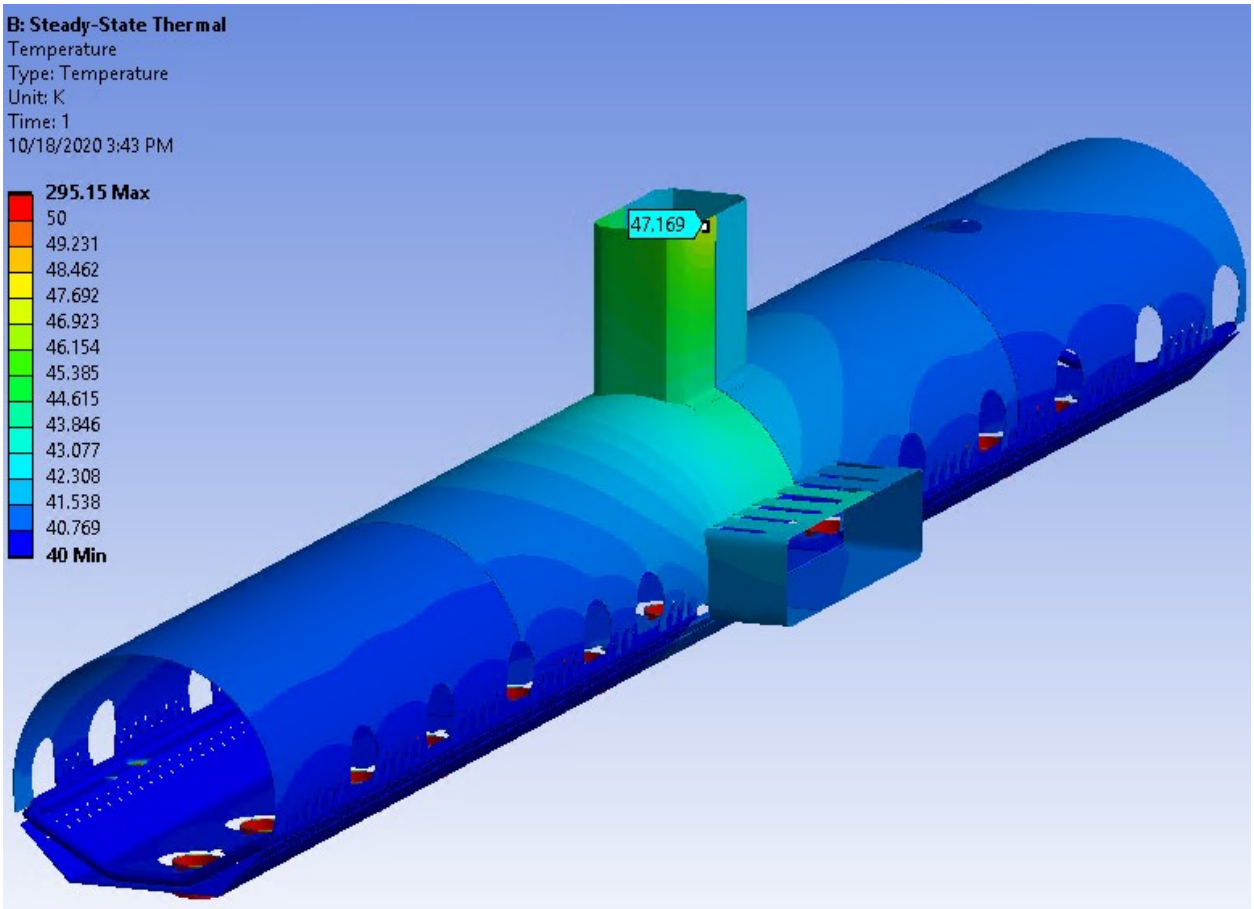

Figure 49 - Steady state thermal temperature map

4.3 Transient Thermal

Transient thermal simulation provides the temperature map for any moment in time during the cooldown process but is not an end unto itself. Results will be imported into the structural analysis and used to compute thermal strain. A structural analysis will be computed for each imported temperature map. Time steps in seconds are specified and the temperature distribution snapshots are created. Each temperature snapshot becomes one timestep for static structural analysis. Any number of static structural simulations can be performed. Temperature distribution at the moment of maximum stress is shown in Figure 50. A close-up view in Figure 51 shows the temperature difference in the critical region to be roughly 14K.

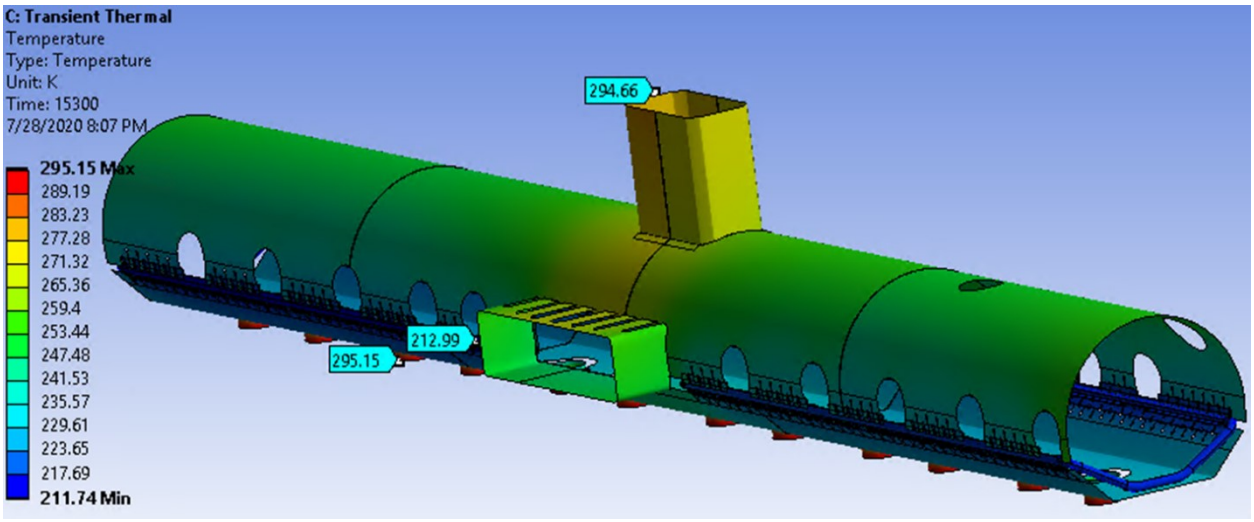

Figure 50 - Temperature distribution at the moment of maximum stress (HB650)

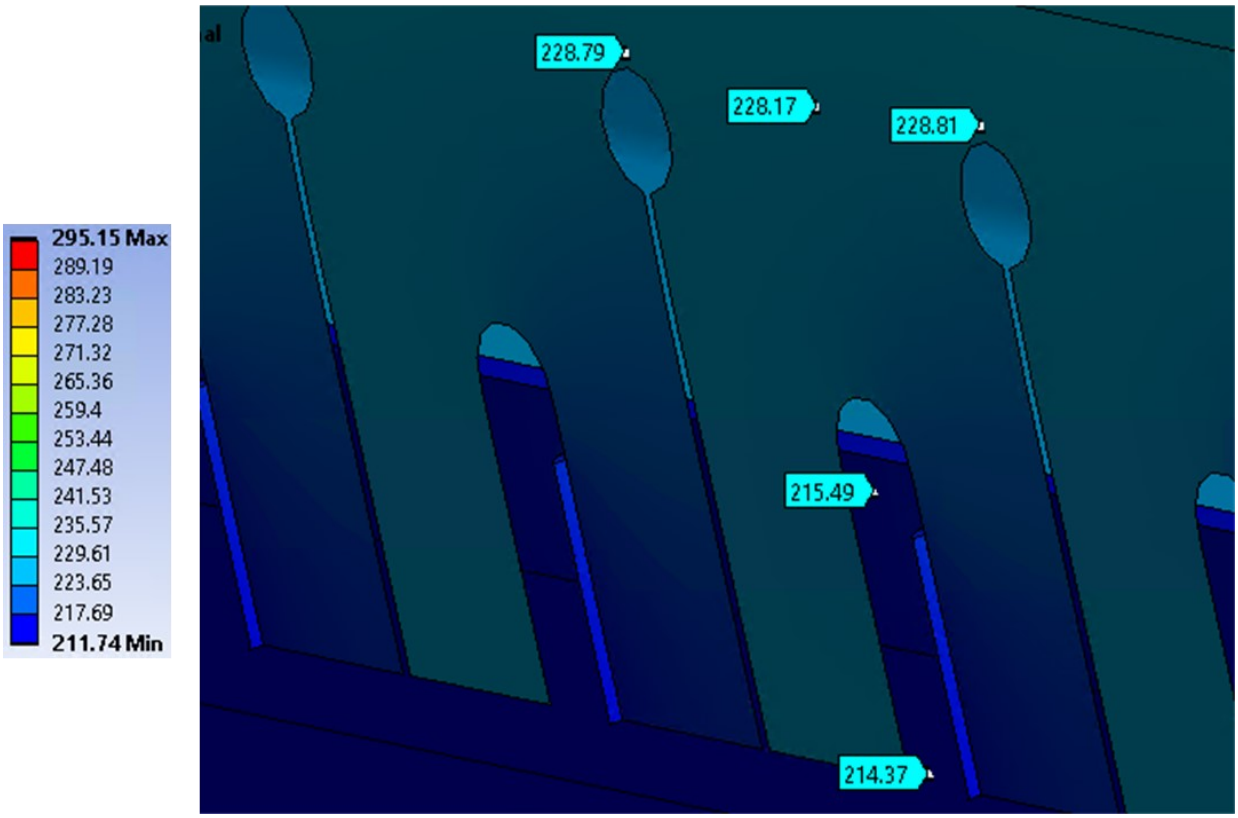

Figure 51 - Temperature distribution in the critical region

4.4 Static Structural

The revised design with weld on just one side of the slot and a cooling at a rate of 20K/hr was selected for implementation on the prototype HB650. Figure 52 shows stress below 30 MPa in all locations of the thermal shield except the concentrations around welds. Figure 53 shows a close-up view showing stress in the welds. A stress singularity appears in this simulation as well. Attempts to modify weld joint geometry to eliminate singularities was unsuccessful. A convergence study found peak stress of 250 MPa. Neuber correction shows equivalent true stress of 80 MPa. MCB life calculations show the 50th percentile of 1000 cycles while SWT showed 800 cycles.

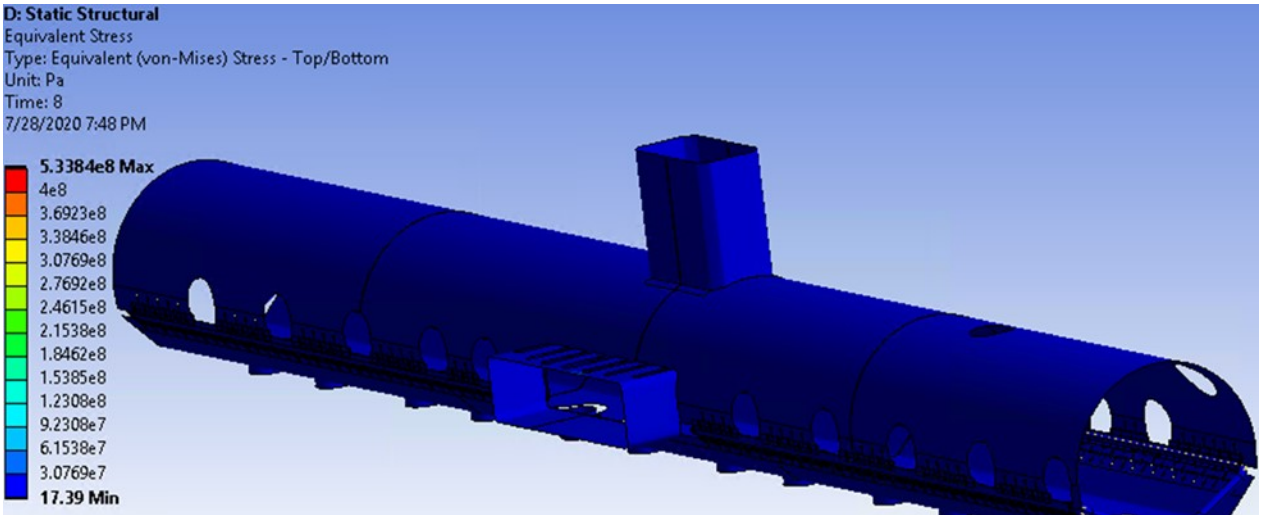

Figure 52 - Peak stress values at 20K/hr

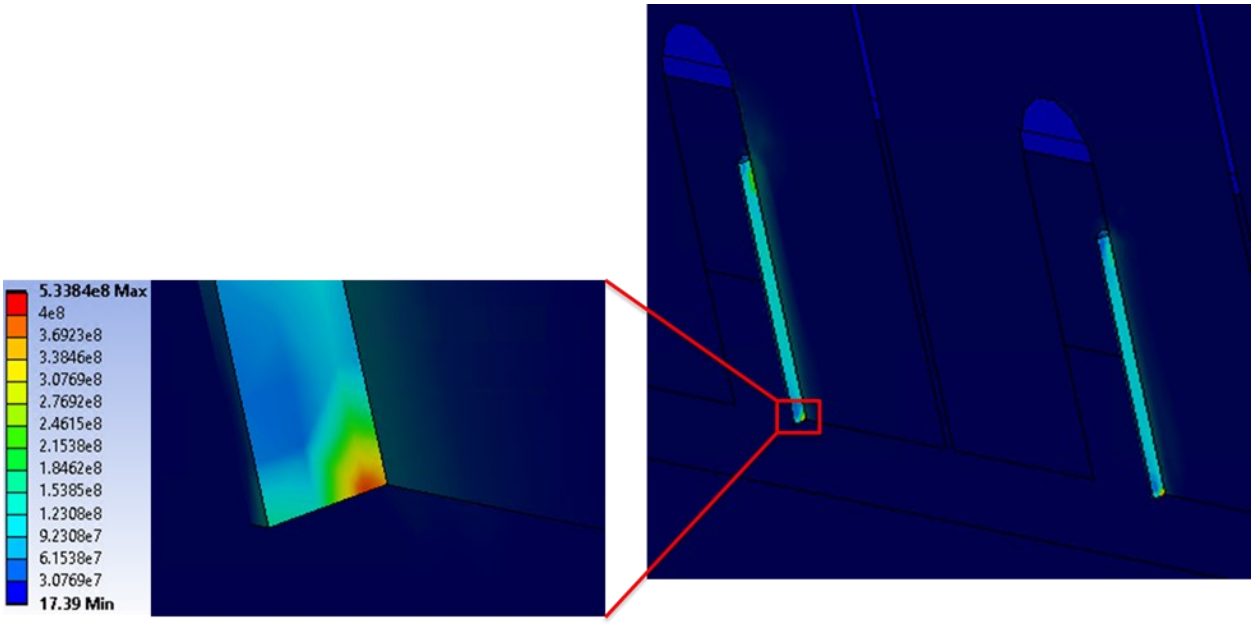

Figure 53 - Peak stress values at 20K/hr close-up

An attempt was made to replace specific shell bodies with solid bodies to eliminate stress singularities. The results were not spectacular and consumed large amounts of precious computer memory. Only select weld joints could be modeled in this manner and those were selected based on locations of maximum stress in the original simulation with shield panels modeled as shell bodies. Solid bodies have 3 degrees of freedom in the axial directions (x,y,z) while shell bodies have 3 axial degrees of freedom plus 3 rotational degrees of freedom, one around each axis. Connecting line bodies, shell bodies and solid bodies with another type is connecting different mathematical frames of reference. In terms of efficiency of simulation line bodies use the least amount of computing resources and solid bodies use the most. The goal of making an accurate simulation might require solid bodies, but equivalent results can often be obtained more efficiently using shell or line bodies. Experimentation of this type was performed on the original design with welds on both sides of the slot. The simulation of a 40K/hr cooling rate showed a 15 K temperature difference in the critical region and peak stress of

164MPa as shown in Figure 54. Neuber correction to equivalent true stress is 71 MPa and MCB strain life was 4000 cycles.

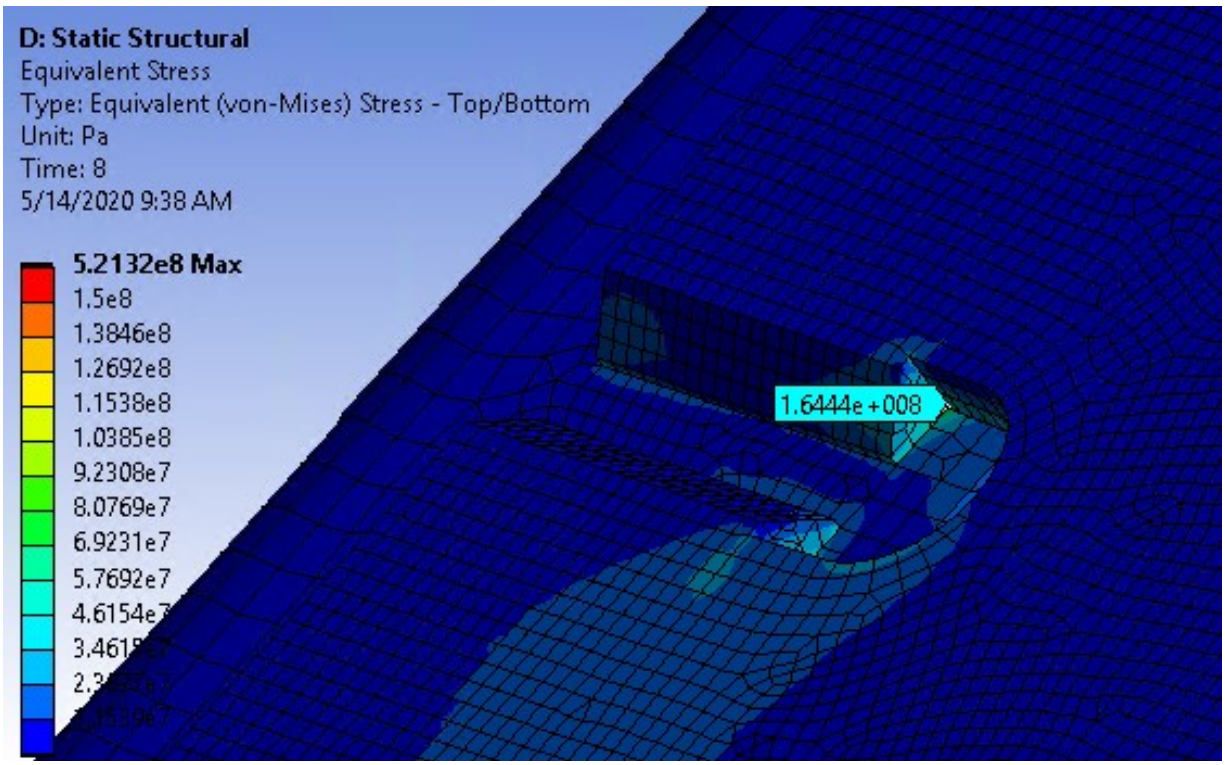

Figure 54 - Peak stress values at 40K/hr

4.5 Structural Buckling

Additional analysis of the thermal shield has been requested in the form of structural buckling. Euler column and beam buckling are computational problems where the critical compressive force applied to a structure that will lead to sudden failure. A beam's length is much greater than the height or width and the problem has a one-dimensional characteristic. The heat exchange pipe shrinks cools and shrinks before shield panels and will therefore be in tension rather than compression. We can forgo this particular analysis.

Plate or membrane bucking similarly seeks to determine the critical compressive or shear force, but the problem lies on a two-dimensional plane. Compressive or shear planar forces in any combination of directions could cause the plate to fail. Simulation in Ansys begins with a static structural solution and calculates the critical stress that would cause the structure to buckle. Several attempts have been made to setup and run a buckling simulation, but the model is simply too large and memory requirements are exceeded.

As previously shown, static structural stress in the shield panels is concentrated at the connection points. The scale for Von Misses stress in Figure 55 has been adjusted to highlight the stress state within the panels. Similarly, the plot of maximum shear stress is shown in Figure 56 with the maximum value outside the fingers less than 10% of yield strength. Compressive stress in the shield panels is near zero as shown in Figure 57. Given loading conditions and state of stress, buckling is an unlikely failure mode.

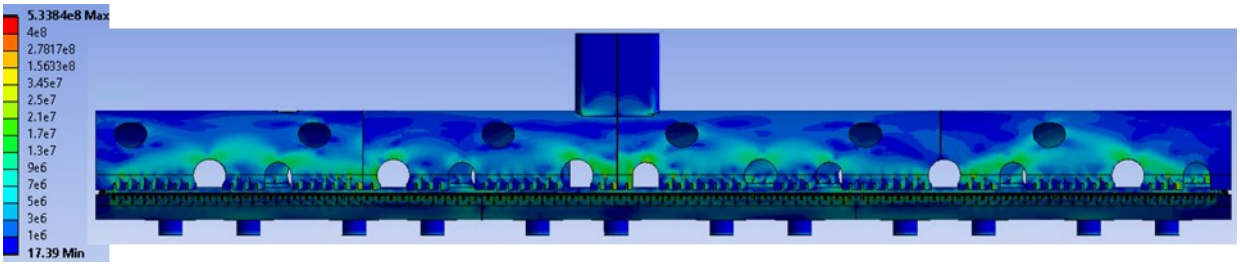

Figure 55 - Maximum Von Misses stress at 20K/hr for HB650 with one side welded

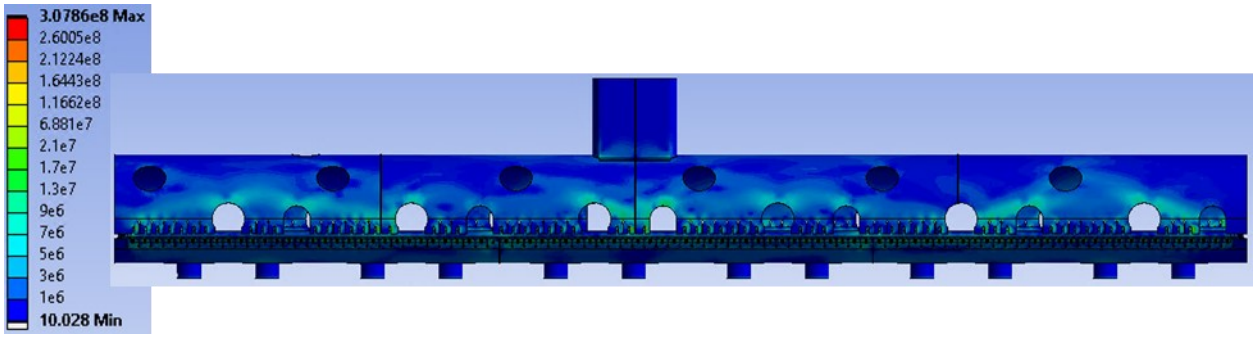

Figure 56 - Maximum shear stress at 20K/hr for HB650 with one side welded

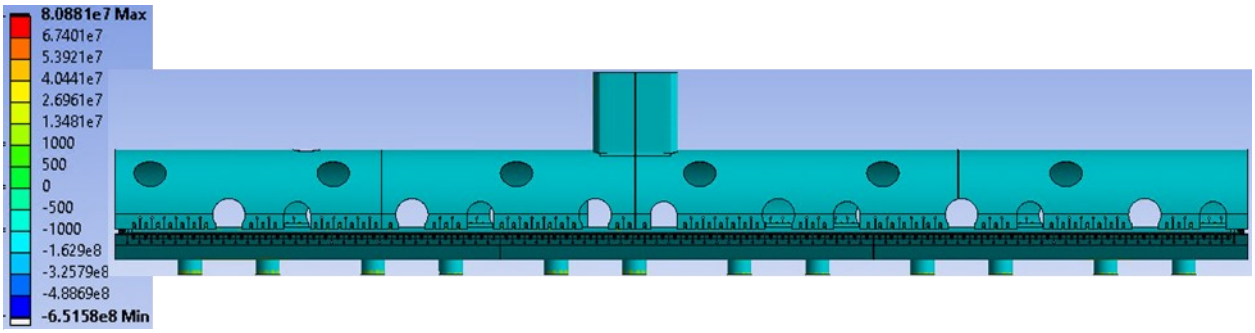

Figure 57 - Maximum compressive stress at 20K/hr for HB650 with one side welded

4.6 Conclusion

A request was made to review the current design strategy and additional proposals were sought for an updated thermal shield design. Cryomodule prototype design had commenced and was mature, so modifications were to be limited in scope due to the impact on other cryomodule components. The specifications for design included preliminary physical dimensions for the device, a requirement for a minimum of 50 thermal cycles, and helium gas refrigerant. A cooling cycle was defined as starting at room temperature, cooling to operating temperatures, and then warming to room temperature again. Additionally, a cooling rate, defined as a change in temperature of the supplied helium gas refrigerant from 296K to 40K, was to be 20 Kelvin per hour or greater.

A cooling rate of 40K/hr is achievable when the optimal design with weld on both sides of the slot are welded. Maximum stress for this configuration will permit an average of 4000 cycles of life. To achieve a cooling rate of 20K/hr, only one side of the slot will be welded. Stress for this configuration is higher but will allow an average of 800 cycles of life. This was the selected design and offered an improvement over the previous design for SSR1 which offered 390 cycles of life at 5K/hr. Life calculations are an estimate of real-world results. The variability in materials, processes, tolerances, and

other real-world factors produce a statistical distribution of the actual number of cycles to failure. A design target can be selected to ensure a high probability of success for achieving 50 thermal cycles.

4.7 Future work

Future work will include physical testing of 1100 and 6061 welded samples to confirm FEA results. Microhardness and tensile testing of welded samples would allow refinement of the assumptions and better estimation of stress, strain, and life. Literature review provided no insight into the change in conductivity or resistance of weld from the base materials. No weld thermal resistance was included in the FEA model, but the question remains unanswered. Physical testing to determine any change in conductivity between base metal and weld metal for the entire operating range should be performed. Thermal conductivity or resistance between members connected with bolts was not included in the FEA model. Physical testing to estimate thermal resistance in bolted connections should also be performed. Peak stress typically occurs between 210 and 240 Kelvin. Testing for the purpose of determining the Ramberg-Osgood constants at those temperatures would improve the accuracy of simulation and life calculations.

References

[1] Fermilab National Accelerator Laboratory, "PIP-II Particle Accelerator," Fermilab National Accelerator Laboratory, Batavia, IL, 2020.

[2] Fermilab National Accelerator Laboratory, "DUNE at LBNF," 25 9 2020. [Online]. Available: https://lbnf-dune.fnal.gov/.

[3] Y. Fukuda and et. al., "Measurements of the Solar Neutrino Flux from Super-Kamiokande's First 300 Days," in *Physical Review Letters*, 1998.

[4] P. Lebrun and L. Tavian, "Cooling with Superfluid Helium," *Research Gate Publication,* 2015.

[5] C. Grimm, Interviewee, *PIP-II Thermal Shield.* [Interview]. 25 September 2019.

[6] S. Cheban, "Thermal Analysis of the 35-50K Shielding for SSR1 Cryomodule," Fermi National Accelerator Laboratory, Batavia, 2018.

[7] S. Gilankar, A. Tiwari, A. Jain, R. Ghosh and K. Mandloi, "Design Note on 70K Thermal Shield of Standalone Cryomodule for 0.92 β 650 MHz SCRF," Cryo-engineering and Cryomodule Development Division, RRCAT, INDIA, Indore, 2019.

[8] The Aluminum Association, Inc., Aluminum Design Manual, Arlington, VA: The Aluminum Association, Inc., 2015.

[9] Matweb, LLC, 1996-2020. [Online]. Available: http://www.matweb.com/index.aspx.

[10] R. Ambriz and Jaramillo, D, "Mechanical Behavior of Precipitation Hardened," DOI 10.5772/58418, 2014.

[11] V. Malin, "Study of Metallurgical Phenomena in the HAZ of 6061-T6 Aluminum Welded Joints," *Welding Journal,* pp. 305-318, 1995.

[12] M. H. Sadd, Elasticity - Theory, Applications, and Numerics, London: Elsevier, 2021.

[13] D. W. Spring, G. Edrissa, S. Aaron, C. Jeffrey and P. Charles, "On the Applicability of Neuber's Rule for Low Cycle Fatigue," in *Proceedings of the ASME 2016 Pressure Vessels and Piping Conference*, Vancouver, 2016.

[14] W. Guo, C. H. Wang and L. R. F. Rose, "Elastoplastic Analysis of Notch-Tip Fields," DSTO Aeronautical and Maritime Research Laboratory, Melbourne, 1998.

[15] S. S. Manson, "Fatigue: A Complex Subject - Some Simple Approximations," National Aeronautics and Space Administration, Cleveland, 1964.

[16] K. N. Smith, P. Watson and T. H. Topper, "A Stress-Strain Function for the Fatigue of Metals," *Journal of Materials,* vol. 5, no. 4, pp. 767-778, 1970.

[17] University of Waterloo, Professor Tim H. Topper, "Fatigue Design - Evaluation Committee of the SAE," April 1999. [Online]. Available: https://fde.uwaterloo.ca/. [Accessed 2019].

[18] C. L. Shen, P. H. Wirsching and G. T. Cashman, "Design Curve to Characterize Fatigue Strength," *Journal of Engineering Materials and Technology,* vol. 118, pp. 535-541, 1996.

[19] D. G. Friend, R. D. McCarty and V. D. Arp, "Thermophysical Properties of Helium-4 from 0.8 to 1500 K with Pressures to 2000 MPa," National Institute of Standards and Technology , Gaithersburg, MD, 2017.

[20] F. P. Incropera, D. P. Dewitt, T. L. Bergman and A. S. Lavine, Principles of Heat and Mass Transfer, Wiley, 2017.

[21] E. D. Marquardt, J. P. Le and R. Radebaugh, "Cryogenic Material Properties Database," in *11th International Cryocooler Conference*, Keysotne, CO, 2000.

[22] J. Fourier and A. Freeman, Analytical Theory of Heat, London: Cambridge University Press, 1878.

[23] R. Ambriz , G. Barrera , R. García and V. López , "Effect of the Weld Thermal Cycles of the Modified Indirect Electric Arc on the Mechanical Properties of the AA6061-T6 Alloy," *Welding International,* pp. 42-51, 2010.

[24] Materials Algorithms Project, "Program Library," [Online].

[25] Fermilab National Accelerator Laboratory, 25 9 2020. [Online]. Available: https://pip2.fnal.gov/.

[26] T. Nicol, Artist, *SSR1 Cryomodule PIP-II.* [Art]. Fermilab, 2019.

[27] T. Nicol, Artist, *SSR1 Cryomodule PIP-II.* [Art]. Fermilab, 2020.

[28] L. Lari, F. G. Garcia, Y. He, I. Kourbanis, N. V. Mokhov, E. Pozdeyev, I. Rakhno, F. Cerutti and L. S. Esposito, "FLUKA-MARS15 Simulations to Optimize the Fermilab PIP-II Movable Beam Absorber," JACoW Publishing, Melbourne, 2019.